High-Frequency Instability of the Sheath-Plasma Resonance

R. L. Stenzel

Department of Physics, University of California
Los Angeles, CA 90024-1547

NAGW-1570

ABSTRACT

Coherent high-frequency oscillations near the electron plasma frequency ($\omega \lesssim \omega_p$) are generated by electrodes with positive dc bias immersed in a uniform Maxwellian afterglow plasma. The instability occurs at the sheath-plasma resonance and is driven by a negative rf sheath resistance associated with the electron inertia in the diode-like electron-rich sheath. With increasing dc bias, i.e. electron transit time, the instability exhibits a hard threshold, downward frequency pulling, line broadening and copious harmonics. The fundamental instability is a bounded oscillation due to wave evanescence, but the harmonics are radiated as electromagnetic waves from the electrodes acting like antennas. Wavelength and polarization measurements confirm the emission process. Electromagnetic waves are excited by electrodes of various geometries (planes, cylinders, spheres) which excludes other radiation mechanisms such as orbitrons or beam-plasma instabilities. The line broadening mechanism has been identified as a frequency modulation via the electron transit time by dynamic ions. Ion oscillations at the sheath edge give rise to burst-like rf emissions. These laboratory observations of a new instability are important for antennas in space plasmas, generation of coherent beams with diodes, and plasma diagnostics.

I. Introduction

The sheath-plasma resonance is a well-known phenomenon of rf probes and antennas in plasmas.[1-3] Basically, an electron-depleted sheath acts like a capacitor ($\epsilon = \epsilon_0$) while a field-free cold plasma can behave inductively ($\epsilon = 1 - \omega_p^2/\omega^2 < 0$ for $\omega < \omega_p$) such that a series resonance is possible. Such resonances have been observed in the rf current to probes,[4] in impedance measurements of antennas,[5] in the thermal emission spectrum from antennas,[6] and in the rectified current of rf signals applied to electrodes in plasmas.[1] Most of these studies were performed for ion-rich sheaths since floating probes or antennas are usually charged negatively with respect to the plasma potential. However, in certain situations antennas can also be charged positively, for example on spacecraft emitting beams,[7] on long tethers,[8] and on antennas and probes driven by large amplitude signals.[9] Few investigations have been performed on the rf behavior of electron-rich sheaths. It is surprising that only recently an important instability of an electron-rich sheath has been observed.[10] The present paper gives a detailed description of this sheath-plasma instability.

Research on vacuum diodes has a long background compared to that on plasma sheaths, but both areas are strongly related.[11] For example, a vacuum-tube electron diode has properties similar to those of an electron-rich (i.e. ion-depleted) plasma sheath, except in the latter case the cathode is not a rigid electrode but a dynamic plasma starting at the sheath edge. The high-frequency properties of diodes differ from the dc behavior due to the finite electron transit time from cathode to anode. The classical analysis by Llewellyn[12] shows that the equivalent rf impedance of a diode can develop a negative differential resistance as a function of electron inertia. When an rf resonator is coupled to the diode the system turns into an active

"monotron" oscillator which had been observed prior to the theoretical understanding.[13]

Plasma sheaths have been studied extensively in theory,[14] computer simulations[15] and laboratory experiments.[16] The analogy between transit- time effects for diodes and plasma sheaths has been pointed out in the case of ion-rich sheaths.[17] Experiments on the ac sheath impedance have shown ion inertia effects at frequencies above the ion plasma frequency but no instabilities were observed or expected due to the lack of a resonant system.[18] For the electrons, however, there exists a natural resonance between the sheath and the ambient plasma. The quality factor of the sheath-plasma resonance is determined by the real part of the rf sheath impedance. When the sheath resistance becomes negative the sheath-plasma resonance spontaneously oscillates. This effect has been observed and is the subject of the present paper.

After describing in Section II the experiment and the measurement techniques, the observations of the instability are presented in the various subsections of Sec. III. The Conclusion, Section IV, points out the relevance of the instability to various applications and distinguishes it from other proposed instability mechanisms.[19,20]

II. Experimental Arrangement

The experiment (see Fig. 1) is performed in a large volume (1 m diam., 2 m length), uniform ($n/\nabla n \simeq 10m$), quiescent ($\delta n/n \lesssim 1\%$), collisionless ($\nu/\omega_p < 10^{-3}$), Maxwellian afterglow plasma ($n_e < 5 \times 10^{11}$ cm^{-3}, $kT_e \simeq 10\ kT_i < 3$ eV, Argon, $p \lesssim 3 \times 10^{-4}$ Torr) produced by a pulsed dc discharge (40 V, 500 A, $t_{on} \simeq 3$ msec, $t_{rep} \simeq 0.5$ sec) with a 1 m diam. oxide-coated cathode.[21] For improved uniformity a weak axial magnetic field ($B_o \simeq 5$ G) is applied which,

for high frequency phenomena, leaves the plasma essentially unmagnetized ($\omega_p^2/\omega_c^2 \approx 10^4$; $\omega_c = eB_o/m_e$). Typical plasma parameters measured with Langmuir probes are shown in Fig. 2. The probe data accurate to at most $\pm$ 10% are complemented with other diagnostics, such as test ion acoustic waves which yield kT_e from the measured sound speed, $c_s^2 = kT_e/m_i$, and test electron plasma waves which yield an extremely accurate ($\pm$ 1%) measure for the electron density from the plasma frequency, $\omega_p^2 = ne^2/m_e\epsilon_o$. The latter diagnostics deserves a short description:

A miniature cathode is inserted into the plasma to produce a weak diagnostic electron beam (100 eV, < 1 mA, 2 mm diam.). Its density is adjusted to barely excite the cold beam-plasma instability which occurs at the intersection of the beam dispersion relation ($\omega = kv_b$) and the Bohm-Gross dispersion ($\omega^2 = \omega_p^2 + 3\,k^2v_e^2$). As shown in Fig. 3a the instability frequency differs from the plasma frequency by only 1.5%, hence yields the density far more accurately than Langmuir probes. Fig. 3b shows observed emission lines at different frequencies and the decay curve of the emission frequency vs. afterglow time, $f_{p(t_a)}$. From the slope ($df_p/dt_a \approx$ 2 GHz/10 msec at $t_a \approx$ 5 msec) and the width of the emission line ($\Delta t_a \approx$ 50 μsec, half-width at half maximum) one can see that the emission frequency is determined to within $\Delta f_p/f_p \approx$ 10 MHz/1 GHz = 1% which indicates the excellent reproducibility, quiescence and uniformity of the plasma.

Based on the accurate density diagnostics with the test electron beam one can estimate the accuracy of Langmuir probe data using, for example, from the least perturbing Bohm current, $I_{isat} = 0.5\ A\ n\ e\ (kT_e/m_i)^{1/2}$, where A is the area of the plane probe.[22] The current-voltage characteristic is swept rapidly compared to the plasma decay time, the electron temperature kT_e is obtained from the electron retardation region near the floating

potential while the ion saturation current is the extrapolated ion current at the plasma potential. The comparison shows that the Bohm current yields to within $\pm$ 2% the same density as the plasma line provided the empirical Bohm factor of 0.5 is replaced by the value 0.43. Without this correction the probe error is (0.5 - 0.43)/0.5 = 14%. There are only very few experiments which determine the density accurately enough to perform such checks.[23]

The high-frequency properties of the various antennas/rf electrodes shown in Fig. 4 have been investigated. All structures are connected via 50Ω coaxial cables to external equipment. The balanced electric dipole has a length $2\ell \approx 4$ cm large compared with the typical Debye length, $\lambda_D \approx 50$ μm, but shorter than the free space electromagnetic wavelength, $\lambda_o \approx 10$ cm. Unbalanced rf antennas consist of cylindrical wires, spherical monopoles, and plane disks of square and circular shapes, the latter insulated on one side. The purpose of choosing different antenna geometries is to examine whether the observed radiation is due to orbitron[24] or beam-plasma instabilities[25] which can only occur for thin wires, or a sheath instability which can occur for any geometry.

The antenna properties are measured with the two basic setups shown in Fig. 5. Sheath-plasma resonances are identified in an active reflection measurement in which a small-amplitude microwave signal is incident on the antenna. The reflected signal is monitored vs. time as the decaying density sweeps out the resonance at a fixed signal frequency. Although this simple setup does not yield the complex antenna impedance it clearly shows the presence of the sheath-plasma resonance in the reflected power and its variation with dc bias, i.e. sheath thickness. The dc bias voltage ($-150V < V_{dc} < +150V$) is applied via a stub tuner ($\lambda/4$ transformer), isolated from

the measurement circuit by a waveguide section, and is only pulsed on the afterglow since during the discharge the thin wires melt from drawing electron saturation current. Instabilities at the sheath-plasma resonance are monitored with a passive microwave receiver consisting of a low-noise broadband preamplifier, mixer, local oscillator, narrowband i.f. amplifier and video detector (spectrum analyzer), and a digital oscilloscope triggered at the repetition rate of the pulsed experiment. The receiver is sensitive enough to observe the thermal noise of the afterglow plasma which has been reported earlier.[6] The receiver is also connected to an external microwave horn antenna (see Fig. 1) so as to observe the far-field electromagnetic radiation from sheath-plasma instabilities.

III. Experimental Results and Interpretation

A. Sheath-Plasma Resonances and Instability

Fig. 6 shows the properties of the sheath-plasma resonance for both ion-rich and electron-rich sheaths. At a fixed frequency (f = 1.09 GHz) the reflected wave amplitude from a spherical electrode is displayed versus afterglow time (bottom scale) or normalized frequencies (top scales) at different dc bias voltages V_{dc} relative to the plasma potential ($V_{p\ell} \simeq +2V$). For ion rich sheaths (Fig. 6a) one observes the expected bias- dependent series resonance and the fixed parallel or antiresonance ($\omega \simeq \omega_p$).[3] The series resonance arises when the spherical sheath capacitance $C_s = 4\pi\epsilon_o (r + s)r/s$ and the surrounding plasma capacitance $C_p = 4\pi\epsilon_o(1 - \omega_p^2/\omega^2)(r + s)$ cancel which occurs at $\omega_p^2/\omega^2 = 1 + r/s$. Thus, for a probe of fixed radius r an increase in sheath thickness s due to a larger negative bias shifts the resonance to decreasing values of ω_p^2/ω^2, i.e. later afterglow times, as is observed. At the plasma potential the sheath collapses and the resonance

vanishes. For positive dc bias (Fig. 6b) a sheath-plasma resonance is seen to emerge where the parallel resonance vanished. With increasing positive bias the resonance becomes stronger, narrower and develops fluctuations beyond a certain threshold bias ($V_{dc} \approx 30$ V). A close inspection of the reflected signal (see insert in Fig. 6b) exhibits an interference pattern near resonance as if a second tuned signal sweeps through the applied signal frequency.

When the positively biased sphere is connected to the passive receiver one observes the results shown in Fig. 7. Above a threshold bias the antenna generates spontaneously a monochromatic oscillation with amplitude growing rapidly with V_{dc} and a line shift toward earlier afterglow times, i.e. larger normalized densities ω_p^2/ω^2 or lower normalized frequencies ω/ω_p. Switching back to the reflection measurements one can see that at the same dc bias ($V_{dc} = 135$ V) the spontaneous emission line and the reflection feature (bottom trace of Fig. 7) exactly coincide which explains the interference effect in Fig. 6b. This coincidence holds for any voltage and for other rf probes, too, with Fig. 8 presenting a further example. It shows reflection and emission at the same frequency and for identical plasma parameters for a miniature sphere ($r \approx 0.1$ mm $\approx 3\ \lambda_D$) and adds an evaluation of the frequency pulling with dc bias. The results clearly show that the instability always occurs at the sheath-plasma resonance.

The dependence of the instability amplitude V_{rf} on dc bias V_{dc} is displayed in Fig. 9 for two different electrodes, a sphere (as in Fig. 7) and a cylinder. Both cases exhibit threshold, growth and saturation. The rf voltage and power ($V_{rf} \approx 0.5$ mV, $V_{rf}^2/50\Omega \approx 5 \times 10^{-9}$ W) saturate at levels small compared to the dc voltage and power, respectively ($V_{dc} \approx 50$ V, $P_{dc} \approx 10^{-4}$ W for the wire). Although this estimate does not include

nonlinear effects such as line broadening and harmonic generation, to be presented below, it is evident that the instability is not of interest for applications requiring a high conversion efficiency. Similarly low efficiencies have been reported for earlier experiments.[20,25]

B. Physical Model of the Instability

The qualitative features of the observed instability can be explained by the physical model presented in Fig. 10. First, the properties of diodes at high frequencies where electron transit time effects become important are recalled (Fig. 10a). To first order, the diode can be represented as a capacitance C in parallel with a conductance G both of which depend on transit time angle $\omega\tau$ as given by the Llewellyn equation.[11,12] The inertia of electrons streaming from cathode to anode increases the capacitance compared to the value C_o in vacuum, and decreases the differential conductance $G = \partial I/\partial V$ until changing its sign at $\omega\tau \geq 2\pi$ and giving rise to a possible instability.

Like the diode an electron-rich plasma sheath (Fig. 10b) is a region of streaming electrons bounded by a cathode (field-free plasma) and a positive anode (antenna). Since the electron transit time τ through a sheath is on the order of the plasma period ($\lambda_D/v_e = \omega_p^{-1}$) the sheath conductance near the plasma frequency is expected to change sign. Assuming the potential profile in a plane sheath to be given by Child-Langmuir's law, $\phi_{(x)} = V_{dc}(x/s)^{4/3}$, with sheath thickness $s = \lambda_D(eV_{dc}/kT_e)^{3/4}$, one finds for the electron transit time

$$\tau = \int_0^s \frac{dx}{(2e\phi_{(x)}/m)^{1/2}} = 3\left(\frac{eV_{dc}}{kT_e}\right)^{1/4} \omega_p^{-1}.$$

An instability near the plasma frequency ($\omega_p\tau > 2\pi$) can arise for dc voltages exceeding $V_{dc} \gtrsim (2\pi/3)^4\, kT_e/e \simeq 19\, kT_e/e \simeq +10$ V at $kT_e \simeq 0.5$ eV. Since the

sheath-plasma interface provides a natural resonance the instability frequency is well defined. The observed frequency pulling toward lower normalized frequencies ω/ω_p is explained by the increase in sheath capacitance with V_{dc} or $\omega\tau$. For cylindrical geometry the calculated transit time is longer than for plane electrodes,[26] which explains the observed low threshold voltage for thin wires (e.g. see Fig. 9). The saturation amplitude is governed by the balance between growth and loss; the former depends on phase coherence, i.e. symmetrical sheaths, uniform density, cold electrons and immobile ions. Losses are due to energy flow into the transmission line and radiation of electromagnetic waves at harmonics of the instability, to be presented below. Low frequency instabilities due to dynamic ions at the sheath edge can modulate the sheath thickness, hence growth rate and rf amplitude.

C. Harmonic Generation

At a given receiver frequency more than one emission line can be observed in the afterglow, an example of which is shown in Fig. 11. With increasing dc bias the number of lines and their width increases until they eventually overlap. First, the mechanism of multiple lines is analyzed, then the line broadening process.

When the receiver frequency is varied the emission lines shift in the afterglow in a manner displayed in Fig. 12. Besides the emission lines the diagram also includes the dependence of the plasma line ($\omega = \omega_p$) vs. afterglow time obtained with the diagnostic electron beam (see Fig. 3). At a given afterglow time, i.e. plasma frequency, the frequency spacing between adjacent emission lines are equal and given by the fundamental frequency of the sheath-plasma resonance. Thus, the instability consists of a fundamental oscillation at the sheath-plasma resonance which is below cutoff

($\omega < \omega_p$), and copious harmonic emissions at $\omega > \omega_p$ which can excite propagating electrostatic and electromagnetic waves.

It is important to note that the emissions above the plasma frequency are not intrinsic instabilities but nonlinear by-products of the fundamental sheath-plasma instability. Harmonics are not seen without the presence of the fundamental and, in contrast to the fundamental, there are no resonances in test wave reflections at the harmonics (see Fig. 8). However, unless the oscillations are observed at the exciter structure or its immediate vicinity ($r < c/\omega_p$) it is easy to miss the presence of the evanescent fundamental and to consider other instability mechanisms which produce electromagnetic or electrostatic waves. The transition from near-zone to far-zone has been explored with a movable receiver antenna identical to the exciter antenna except for the dc bias ($V_{dc} < 0$).

Fig. 13a shows that both the fundamental and the second harmonic exhibit a monotonic amplitude decay in the near-zone. With increasing distance ($r > c/\omega_p \approx 1.6$ cm) the fundamental amplitude truely vanishes while the harmonic remains observable throughout the plasma and beyond. If the harmonic signal were an electrostatic wave Landau damping at $\omega/\omega_p \approx 1.7$ would not allow the short wavelength mode ($\lambda \approx 0.2$ mm, $\lambda_D \approx 3 \times 10^{-2}$ mm) to propagate as far as observed. The harmonic emissions are clearly electromagnetic waves as demonstrated in Fig. 13b which indicates typical electromagnetic wavelengths from the standing wave pattern arising from wave reflections at the metallic chamber wall. The observed wavelength in the plasma (λ_p) is longer than the free-space wavelength (λ_o) consistent with the dispersion relation $\omega^2 = \omega_p^2 + k^2c^2$ and third harmonic emission at $f \approx 2.1\ f_p = 3.6$ GHz.

In order to understand how an electrostatic sheath oscillation excites an electromagnetic wave it is helpful to know the polarization of the

fields. Fig. 14a displays received field amplitudes vs. angles measured with linearly polarized antennas (balanced electric dipole, shielded magnetic dipole).[6] From minima and maxima of $E_{(\theta)}$ and $B_{(\theta)}$ it is concluded that the electric field is parallel to the exciter wire and the magnetic field is azimuthal to it. Thus, the radiation process, schematically shown in Fig. 14b, is identical to that of a driven wire antenna, except that the rf current is not supplied via the transmission line from an external generator but is provided by the collected electrons which are modulated in the oscillating sheath electric field. The harmonics are thought to be generated by bunching of electrons as described by second order analyses for diodes.[11] For unbalanced antenna arrangements the transmission line may contribute to the radiation pattern, otherwise it provides a sink for rf currents and the supply for dc power which drives the sheath oscillator. The observed polarization is inconsistent with other radiation mechanisms proposed for earlier observations of electromagnetic emissions from positively biased wires in plasmas. In orbitron instabilities[19,24] electron bunches orbit around the wire which would produce an rf magnetic field along the wire orthogonal to the observed azimuthal B-field. For mode conversion of two oppositely propagating electron plasma waves[25] driven unstable by overshooting counterstreaming electrons in the sheath region the rf electric field ($\omega \simeq 2\ \omega_p$) should be normal to the wire which is not observed.

The most direct confirmation that the above mentioned instability mechanisms cannot explain the present observations is presented in Fig. 15. Electromagnetic harmonic lines are observed for all basic electrode geometries: plane, cylindrical and spherical. It is inconceivable that long-lived electron orbits or counterstreaming electron beams arise at a large plane electrode, whereas sheath-plasma instabilities can occur for any

electrode geometry. Finally, the influence of a weak dc magnetic field has been investigated. The sheath-plasma instability is observed with and without weak magnetic field ($0 < B_o \lesssim 40G$) for any orientation of the wire with respect to $\vec{B}_o$. These features are more consistent with a bounded sheath oscillation than with a mechanism depending on particle trajectories.

D. Low Frequency Sheath Dynamics

While diodes have a fixed anode-cathode spacing the width of a sheath not only varies with dc bias but may also fluctuate at low frequencies since ions are not immobile. A slow variation of the sheath width and shape will modulate amplitude and frequency of the sheath-plasma instability, hence broaden the emission lines. Such processes occur self-consistently at large dc voltages as shown in Fig. 16.

Fig. 16a shows on an expanded time scale ($3 < t_a < 4.5$ msec) the third harmonic emission from a cylindrical wire at different dc bias voltages. Line shift and broadening vs. time t_a are converted via $\omega_p(t_a)$ to a display vs. normalized fundamental frequency ω_o/ω_p ($\omega_o = \omega/3 = \text{const.}$) and presented in Fig. 16b. Note that extrapolation to $V_{dc} = 0$ yields the plasma density as accurately as Langmuir probes. While the line shift was associated with the increase in sheath capacitance with transit time (see Fig. 10a) the line broadening can arise from related factors such as variations of sheath width along and around the wire due to density, temperature and potential fluctuations which could be produced by current-driven instabilities, ionization, and secondary electrons. While the very broadband cases ($V_{dc} \gtrsim 20$ V) are difficult to analyze the onset of line broadening ($V_{dc} \approx 15$ V) yields useful information about the underlying processes.

Fig. 17 displays an emission line vs. afterglow time on three time scales of vastly different resolution. On the coarse time scale (1 msec/div) only

the envelope of the line is resolved, but on the expanded scales the emission is found to consist of multiple peaks in time. The multiple emissions represent a temporal variation rather than frequency-resolved spectral lines since for the present receiver bandwidth (Δf = 3 MHz) and the plasma frequency decay ($df_p/dt_a \simeq$ 150 MHz/msec) a monochromatic line at $f \simeq 0.8\ f_p$ would be swept out in $\Delta t_a = \Delta f/(df/dt_a) \simeq$ 25 μsec. Thus, the sheath-plasma instability arises in short ($\Delta t \simeq$ 1 μsec), periodic ($t_{rep} \simeq$ 5 μsec) rf bursts. The same low frequency (f ≃ 200 kHz) amplitude modulation is also observed on the dc current collected by the biased wire antenna. The emission maximizes when the electron current is at a minimum.

The low frequency instability and modulation of the rf signal can occur over substantial times in the afterglow. Fig. 18 shows that upon tuning of the receiver frequency the envelope of the high frequency emission shifts with afterglow time ($\omega/\omega_p \simeq$ const.) while the modulation is present everywhere since the low frequency signal is continuous. Some characteristics of the low frequency current fluctuations are summarized in Fig. 19.

Fig. 19a shows the total electron current to the wire antenna vs. afterglow time to indicate the relative fluctuation level $\delta I_e/I_e$ = 1...10%, while Fig. 19b shows the ac current fluctuations vs. afterglow time at different dc bias voltages. The current fluctuations only arise above a density- dependent threshold bias ($V_{dc} \gtrsim$ 12 V) beyond which amplitude and bandwidth grow with V_{dc}. There is no evidence that the low frequency fluctuations are driven by the relatively weak high-frequency sheath-plasma instability; vice versa, the sheath-plasma instability is also observed without low frequency modulations.

The low frequency current fluctuations are thought to be generated by periodic expulsions and backflow of ions near the sheath edge which has been

observed in earlier experiments.[27] Although this topic is not the focus of the present paper it is worth pointing out how a periodic variation of the sheath thickness can modulate the high-frequency signal. As the ions are expelled the sheath expands, the electron transit time increases, the instability threshold is exceeded and rf is emitted. When the ions slosh back the instability is quenched while the collected current assumes a maximum. With increasing dc voltage the frequency pulling during bursts of emission broadens the emission line. Thus, electronic tuning via the sheath capacitance $C(\omega\tau)$ explains the line broadening rather than amplitude modulation which is limited to the ion plasma frequency.

A second experiment has been performed to show the effect of the ion dynamics on the sheath-plasma instability. As indicated in Fig. 20 the dc bias voltage is rapidly switched on ($\Delta t \lesssim 30$ nsec) so as to establish a repeatable transition from an ion-rich to an electron-rich sheath. The normalized frequency ω/ω_p (ω = const.) and relative amplitude V_{rf} of the sheath-plasma instability are displayed vs. delay time from switch-on. As the excess ions are expelled and the sheath expands the electron transit time angle $\omega\tau$ increases, the instability grows and the frequency pulls downward. The frequency pulling ($df/dt \simeq 1.3$ MHz/μsec @ $t_d \simeq 10$ μsec) rather than the slower plasma decay ($df_p/dt \simeq 0.4$ MHz/μsec) now determines the temporal line width ($\Delta t \sim 2.5$ μsec), given the receiver bandwidth ($\Delta f \simeq 3$ MHz). The slow time scale of the sheath adjustment is clearly controlled by the ion dynamics. When the dc bias is turned off the instability decays within the switching time due to the loss of electron current.

IV. Conclusions

Experimental results and a proposed physical model demonstrate the

existence of a new instability associated with electron inertia in plasma sheaths. The high-frequency sheath-plasma instability is not only of intrinsic interest as a basic plasma property but must be understood when using antennas in plasmas. For example, when electron beams are injected from a spacecraft the antennas and other electrodes can charge positively, and the resultant emissions from the sheath-plasma instability could be mistakenly interpreted as beam-plasma instabilities. Similarly, large positive voltages exist on high power antennas, long electrodynamic tethers and space stations. In the laboratory the instability is important for plasma diodes,[28] cathode sheaths, and potentially applicable to plasma diagnostics (density, potential).

The observed properties of the present instability show clearly that the radiation mechanism cannot be explained by earlier models applied to related experiments. For example, parametric decay instabilities of the sheath-plasma resonance[29] require a strong rf pump which is not present in this experiment. Orbitron instabilities[19] require orbiting electrons which are excluded here by a plane probe geometry. Likewise, counterstreaming electron beams[25] are avoided by plane geometry and dc magnetic fields. Thus, the present experiment unambiguously points to a different mechanism, identfied as the sheath-plasma instability. Of course, this does not imply that orbitron or beam-plasma instabilities are not observable in suitably designed experiments but it shows that not every biased wire in a plasma radiates in the same way.

It would be desirable to extend the present experiments to strongly magnetized plasmas ($\omega_c > \omega_p$) which would enrich the features of the instability and enlarge the range of applicability. Ion inertia in ion-rich sheaths should be reexamined for understanding related low frequency instabilities.[30]

Acknowledgments

The author gratefully acknowledges technical assistance from Dr. J. M. Urrutia, valuable discussions with Drs. G. Morales and C. Birdsall, and the expert clerical help from Mrs. S. Proctor. This work was supported in part by the National Science Foundation grants PHY87-13829 and ATM 87-02793, and the National Aeronautics and Space Administration grant NAGW-1570.

REFERENCES

1. K. Takayama, H. Ikegami and S. Miyazaki, Phys. Rev. Lett. 5, 238 (1960).
2. R. S. Harp and F. W. Crawford, J. Appl. Phys. 35, 3436 (1964).
3. G. Bekefi, Radiation Processes in Plasmas (John Wiley, New York, 1965).
4. J. Uramoto, Phys. Fluids 13, 657 (1970).
5. W. Heikkila, in Plasma Waves in Space and the Laboratory, edited by J. O. Thomas and B. J. Landmark, (Elsevier, New York, 1969), Vol. 1, pp. 231-246.
6. R. Stenzel, Phys. Fluids (July, 1989).
7. L. M. Linson, in Artificial Particle Beams in Space Plasma Studies, edited by B. Grandal, (Plenum, New York, 1982), pp. 573-595.
8. P. M. Banks, P. R. Williamson and K.-I. Oyama, Planet. Space Sci. 29, 139 (1981).
9. I. P. Shkarovsky, Radio Science 7, 503 (1972).
10. R. Stenzel, Phys. Rev. Lett. 60, 704 (1988).
11. C. K. Birdsall and W. B. Bridges, Electron Dynamics of Diode Regions, (Academic Press, New York, 1966).
12. F. B. Llewellyn, Electron Inertia Effects (Cambridge Univ. Press, New York, 1941).
13. J. Müller, Hochfrequenztechnik und Elektroakustik 41, 156 (1933).
14. S. A. Self, Phys. Fluids 6, 1762 (1963); J. Appl. Phys. 36, 456 (1965).
15. T. M. Antonsen, Jr., W. H. Miner, E. Ott, and A. T. Dobrott, Phys. Fluids 27, 1257 (1984).
16. R. S. Harp, W. B. Cannara, F. W. Crawford, and G. S. Kino, Rev. Sci. Instrum. 36, 960 (1965).
17. R. Rosa, J. Phys. A: Gen. Phys. 4, 934 (1971).

18. B. M. Oliver and R. M. Clements, J. Appl. Phys. 44, 1128 (1973).

19. I. Alexeff and F. Dyer, Phys. Rev. Lett. 45, 351 (1980).

20. R. W. Schumacher and R. J. Harvey, Bull. Am. Phys. Soc. 29, 1179 (1984); 31, 1601 (1986).

21. R. L. Stenzel and W. F. Daley, U. S. Patent No. 4,216,405 (1980).

22. F. F. Chen, in Plasma Diagnostic Techniques, edited by R. H. Huddlestone and S. L. Leonard, (Academic Press, New York, 1965), p. 150.

23. R. L. Stenzel, Phys. Fluids 16, 565 (1973).

24. I. Alexeff, Phys. Fluids 28, 1990 (1985).

25. R. W. Schumacher and R. J. Harvey, in Proceedings of the 1984 IEEE International Conference on Plasma Science, IEEE Publ. No. 84 CH 1958-8, (IEEE, New York, 1984), pp. 109-110.

26. K. R. Spangenberg, Vacuum Tubes, (McGraw-Hill, New York, 1948), Chap. 8.

27. J. M. Urrutia and R. L. Stenzel, Phys. Rev. Lett. 57, 715 (1986).

28. M. A. Mostrom, R. M. Clark, M. J. Arman, M. M. Campbell, B. D. Godfrey, D. J. Sullivan and J. E. Walsh, Bull. Am. Phys. Soc. 33, 2116 (1988).

29. R. L. Stenzel, H. C. Kim, and A. Y. Wong, Radio Science 10, 485 (1974)

30. J. Chutia and Y. Nakamura, submitted to Phys. Rev. Lett. (1989).

FIGURE CAPTIONS

Fig. 1 Schematic picture of the experimental device.

Fig. 2 Electron density and temperature vs. afterglow time obtained from Langmuir probe measurements.

Fig. 3 Density diagnostics with a test electron beam. (a) Theoretical dispersion diagram ω vs. k for cold beam modes and Bohm-Gross modes predicts an instability at ~ 1.5% above the electron plasma frequency. (b) Beam-plasma instability observed with a narrowband receiver (Δf = 3 MHz) at different frequencies in the afterglow yields the decay of the plasma frequency $f_p(t_a)$. Based on the line width the density is determined accurate to within $\pm$ 1%.

Fig. 4 Schematic picture of antennas and rf probes used to excite the sheath-plasma instability. Typical electrode dimensions are smaller than electromagnetic wavelengths λ_o but larger than Debye lengths, λ_D.

Fig. 5 Experimental arrangement for passive measurements of unstable emissions (top set up) and active reflection measurements of test waves to identify sheath-plasma resonances (bottom set up).

Fig. 6 Identification of sheath-plasma resonances from the reflected signal of test waves applied to a spherical rf electrode. At a fixed frequency the resonances are traced out by the density decay in the afterglow [$\omega_p(t_a)$, see top and bottom scales]. (a) At negative dc bias (V_{dc}) relative to the plasma potential ($V_{p\ell}$) both series and parallel resonances are observed. The resonances vanish when the sheath collapses ($V_{dc} \simeq V_{p\ell}$). (b) For positive dc bias a reflection line emerges near the parallel

resonance. With increasing bias its normalized frequency decreases, the Q-value increases, and spontaneous oscillations arise which produce a beat patttern at resonance (see top insert).

Fig. 7 Emission amplitude vs. afterglow time at different dc bias voltages showing threshold, growth and line shift of the instability. The emission lines exactly coincides with the reflection lines (see example for V_{dc} = 135 V at bottom), hence the sheath-plasma resonance oscillates spontaneously.

Fig. 8 Comparison of reflection lines (a) and emission lines (b) vs. afterglow time at different dc bias voltages for a miniature sphere (r = 0.1 mm $\simeq$ 3 λ_D). (c) Frequency pulling of the sheath-plasma resonance with dc bias voltage.

Fig. 9 Instability amplitude vs. dc bias voltage for rf electrodes of cylindrical and spherical shape. Typical levels of threshold and saturation are V_{dc} = 10...30 V, $V_{rf} \simeq$ 0.5 mV, respectively, indicating a low power conversion efficiency ($P_{rf}/P_{dc} \lesssim 5 \times 10^{-5}$).

Fig. 10 Physical picture of the sheath-plasma instability mechanism. (a) Theory and observations for electron-filled diodes show that at high frequencies electron inertia causes the equivalent diode conductance $G = \partial I/\partial V$ to become negative (transit time angle $2\pi < \omega\tau < 3\pi$) while the equivalent capacitance increases over the vacuum value C_o. (b) The ion-depleted sheath of a positively biased electrode in a plasma behaves qualitatively like a diode except the cathode (sheath edge) is dynamic and the sheath-plasma interface exhibits a natural resonance at $\omega \lesssim \omega_p$. The transit time angle $\omega_p\tau$ depends on normalized dc bias, and instability is possible for $V_{dc} \gtrsim 20\ kT_e/e$. The increase in sheath capacitance with V_{dc} explains the observed

downward frequency pulling.

Fig. 11 Emission lines vs. afterglow time at a fixed receiver frequency for different dc bias voltages. Multiple lines are subsequently identified as harmonic of the sheath-plasma instability which are radiated from the biased wire antenna to a second remote receiver antenna used here. The evanescent fundamental line is not visible. Note line shift and broadening with V_{dc}.

Fig. 12 Emission frequencies vs. afterglow time of multiple lines from a spherical rf electrode. For reference, the plasma frequency $f_p(t_a)$ is also shown. At a given afterglow time the emissions occur at multiples of the fundamental sheath-plasma resonance. Reflection lines (crosses) occur at the fundamental but not at harmonics. S-band and C-band waveguides are used as high-pass filters to ascertain harmonic generation in the sheath rather than in the receiver.

Fig. 13 Spatial variation of the instability amplitude. (a) In the near-zone the fundamental oscillation decays with scale length $c/\omega_p \simeq$ 1.6 cm. The second harmonic ($\omega/\omega_p \simeq 1.7$) couples to long wavelength ($\lambda_o \simeq 10$ cm) electromagnetic modes rather than short wavelength ($\lambda_e \simeq 0.2$ mm), Landau damped ($k_i/k_r \simeq 0.3$) electrostatic modes. (b) In the far-zone ($r > \lambda_o$) the electromagnetic wavelength ($\lambda_p \simeq 9.5$ cm) of the third harmonic ($\omega/\omega_p \simeq 3 \times 0.7$) is obtained from the amplitude standing wave pattern associated with reflections from the chamber wall.

Fig. 14 Polarization of electric and magnetic fields of harmonic emissions. (a) Measured field components E, B vs. rotation angle θ of receiver dipoles adjacent ($r \simeq 10$ cm) to the biased wire. The fields are highly polarized with $\vec{E}$ along the wire, $\vec{B}$ around the

wire axis $\vec{\ell}$. (b) Schematic picture of the radiation mechanism. The electrons collected by the positive wire are modulated by the oscillating sheath electric field. The rf current flowing along the wire into the transmission line excites transverse electromagnetic waves similar to a driven wire antenna. (c) Schematic representation of other proposed mechanism to explain radiation from dc biased wires. The orbitron instability[19] is expected to produce rf magnetic fields along the wire, while nonlinear wave-wave coupling of counterstreaming electron plasma waves[25] generates rf electric fields normal to the wire. Both models are inconsistent with observations.

Fig. 15 Electromagnetic harmonic emission lines from biased electrodes of plane, cylindrical and spherical geometry. The sheath-plasma instability can arise for electrodes of arbitrary shape while other proposed mechanisms[19,25] require cylindrical geometry.

Fig. 16 Frequency shift and line broadening with dc bias voltage. (a) Expanded view of the third harmonic emission line vs. afterglow time at different dc bias voltages and fixed receiver frequency. (b) Line shift and broadening (vertical bar = line width at half maximum) of the normalized fundamental emission frequency ω_o/ω_p ($\omega_o/2\pi$ = 1 GHz = const.) vs. bias V_{dc}. Note that the line width far exceeds the ion plasma frequency ($f_{pi}/f_{pe} \simeq 0.0037$) hence arises from electronic tuning rather than from ion plasma oscillations.

Fig. 17 Fundamental emission line vs. afterglow time displayed on three time scales of vastly different resolution. The sheath-plasma oscillation is observed to be emitted in temporal bursts ($\Delta t \lesssim$ 1 μsec, $t_{rep} \simeq$ 5 μsec) which are phase coherent with low

frequency oscillations in the current to the wire, δI_e, shown in the bottom panel. The process is believed to be due to ion oscillations at the sheath edge which modulate the electron transit time angle, hence instability amplitude.

Fig. 18 Amplitude modulation of the high frequency line by low frequency sheath oscillations. (a) High-frequency sheath-plasma oscillations vs. afterglow time at different receiver frequencies. The envelope which characterizes the line width ($\Delta f \simeq 10$ MHz) shifts with decreasing frequency to later afterglow time since $\omega/\omega_p(t_a) = \text{const}$. At each frequency the pulse modulation is present. (b) Low-frequency current oscillations vs. afterglow time responsible for the modulation of the high-frequency oscillation during most of the afterglow.

Fig. 19 Characteristics of the low frequency sheath oscillations. (a) Electron current collected by the positively biased wire vs. afterglow time, $I_e(t_a)$. Note low level of noise ($\delta I_e/I_e < 10\%$). (b) Filtered current fluctuations vs. afterglow time, $\delta I_e(t_a)$, at different dc bias voltages, V_{dc}. The low frequency instability exhibits a density-dependent threshold and a growth in amplitude and bandwidth with increasing dc bias. Repeated ion expulsion and back flow characterize the plasma dynamics at the sheath edge.[27]

Fig. 20 Rapid switching of the dc bias ($V_{dc}(t_a)$, top trace) creates a controlled, repeatable transition from an ion-rich to an electron-rich sheath. The variation of amplitude V_{rf} and normalized frequency ω/ω_p of the sheath-plasma instability (second trace from top to bottom) is plotted vs. delay time t_d after turn-on (bottom traces), showing implicitely that the growth of the electron-rich sheath is controlled by the slow ion dynamics.

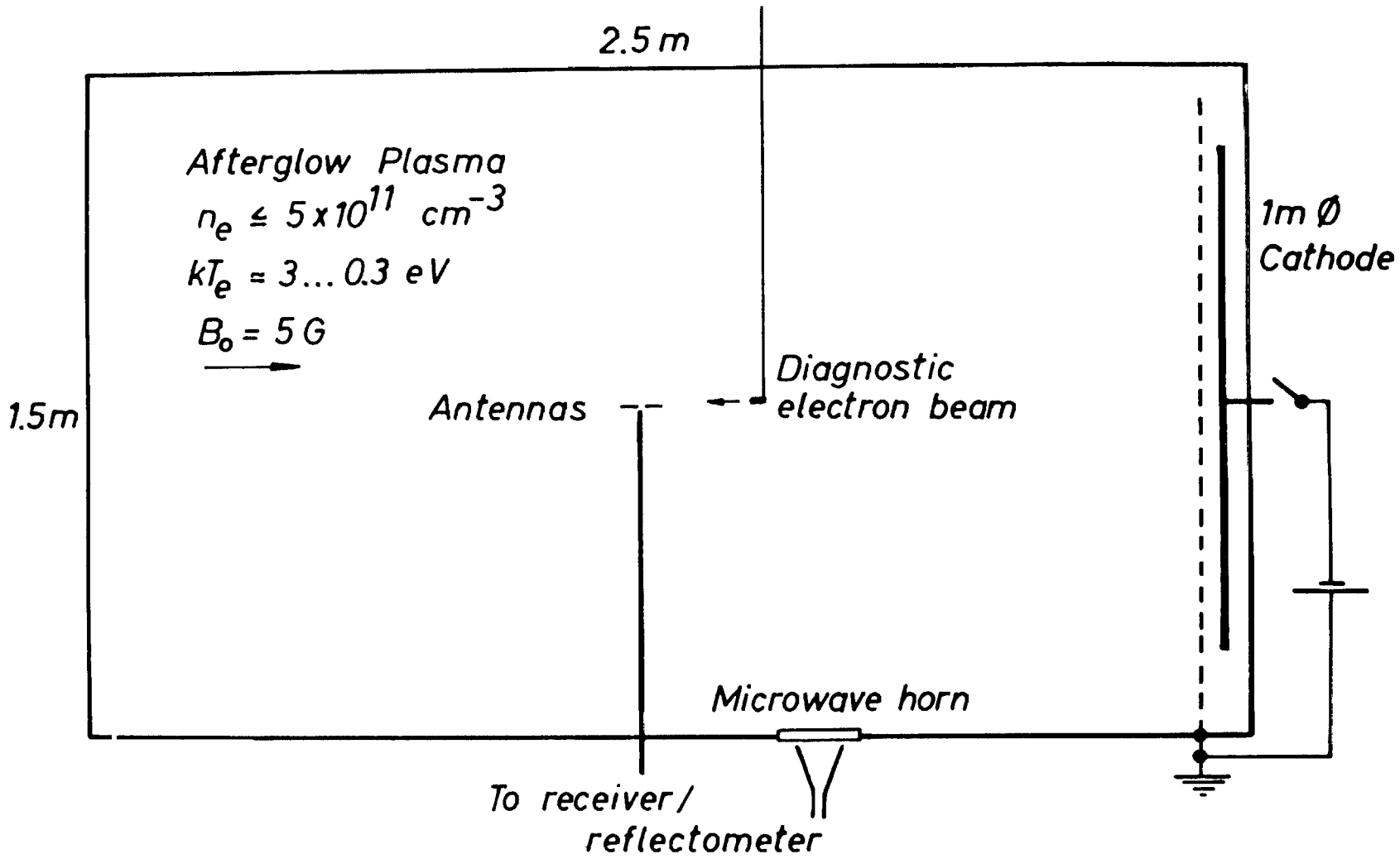
2.5 m
Afterglow Plasma
$n_e \leq 5 \times 10^{11}$ cm^{-3}
$kT_e = 3 \ldots 0.3$ eV
$B_o = 5$ G
1.5m
Antennas
Diagnostic
electron beam
1m Ø
Cathode
Microwave horn
To receiver/
reflectometer

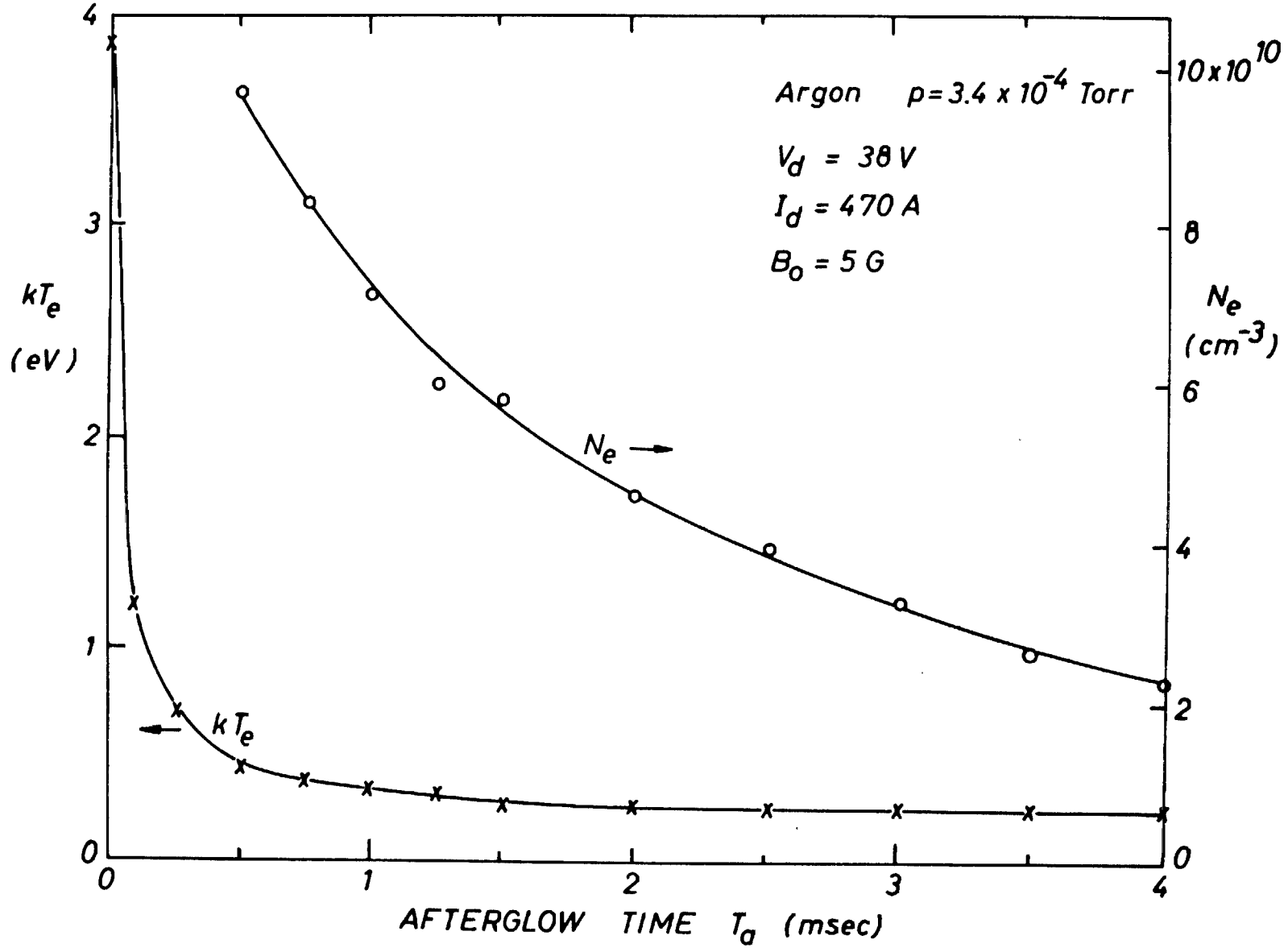
Argon p=3.4 x 10^-4 Torr
V_d = 38 V
I_d = 470 A
B_0 = 5 G
kT_e (eV)
N_e (cm^-3)
10 x 10^10
N_e
kT_e
AFTERGLOW TIME T_a (msec)
0
1
2
3
4
6
8

Fig. 2

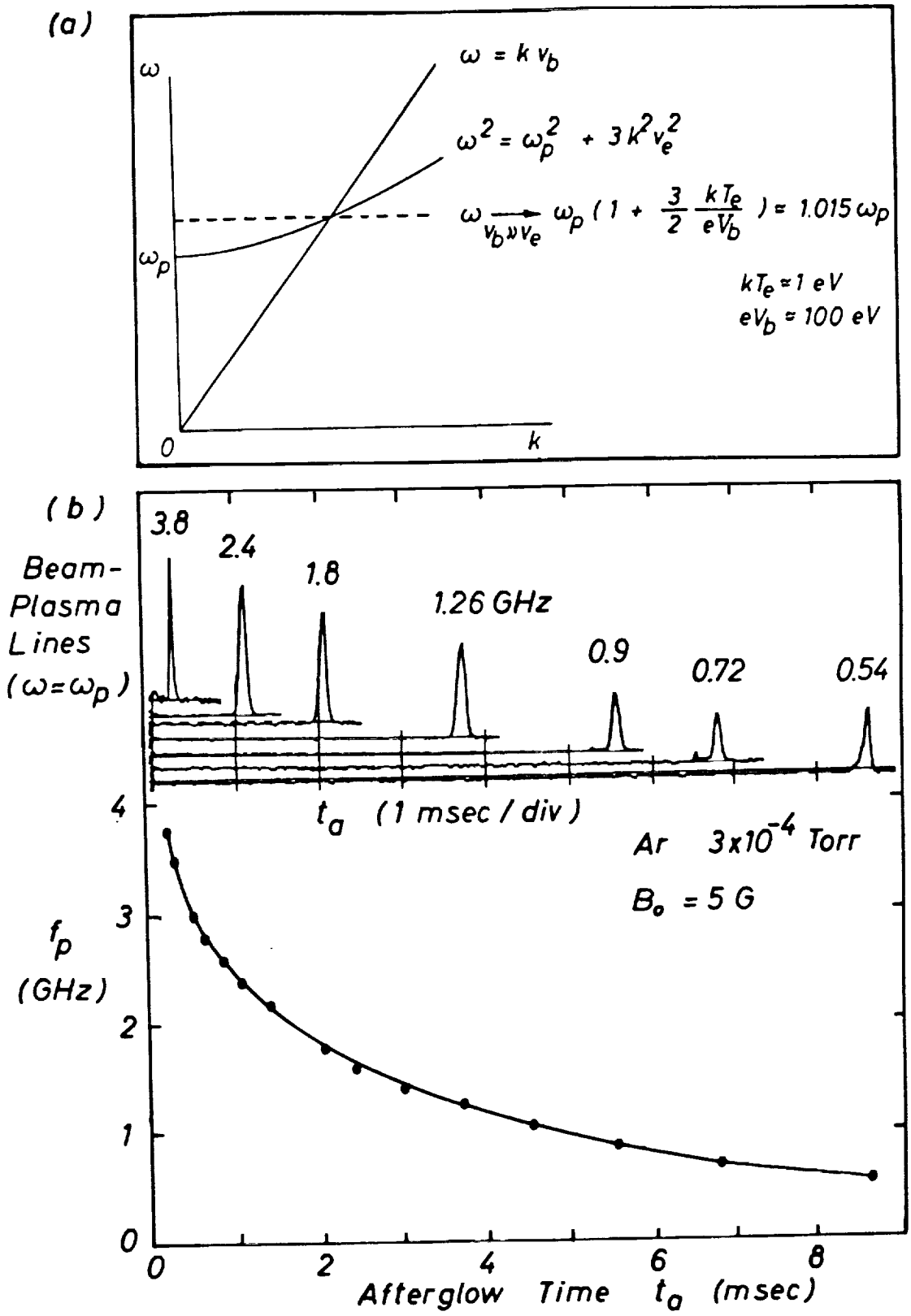
(a)
ω
ω = k v_b
ω² = ω_p² + 3k²v_e²
ω → ω_p (1 + 3/2 kT_e/eV_b) = 1.015 ω_p
v_b ≫ v_e
ω_p
kT_e = 1 eV
eV_b = 100 eV
0
k
(b)
Beam-Plasma Lines (ω=ω_p)
3.8
2.4
1.8
1.26 GHz
0.9
0.72
0.54
t_a (1 msec / div)
Ar 3x10⁻⁴ Torr
B_o = 5 G
f_p (GHz)
4
3
2
1
0
0
2
4
6
8
Afterglow Time t_a (msec)

Fig. 3

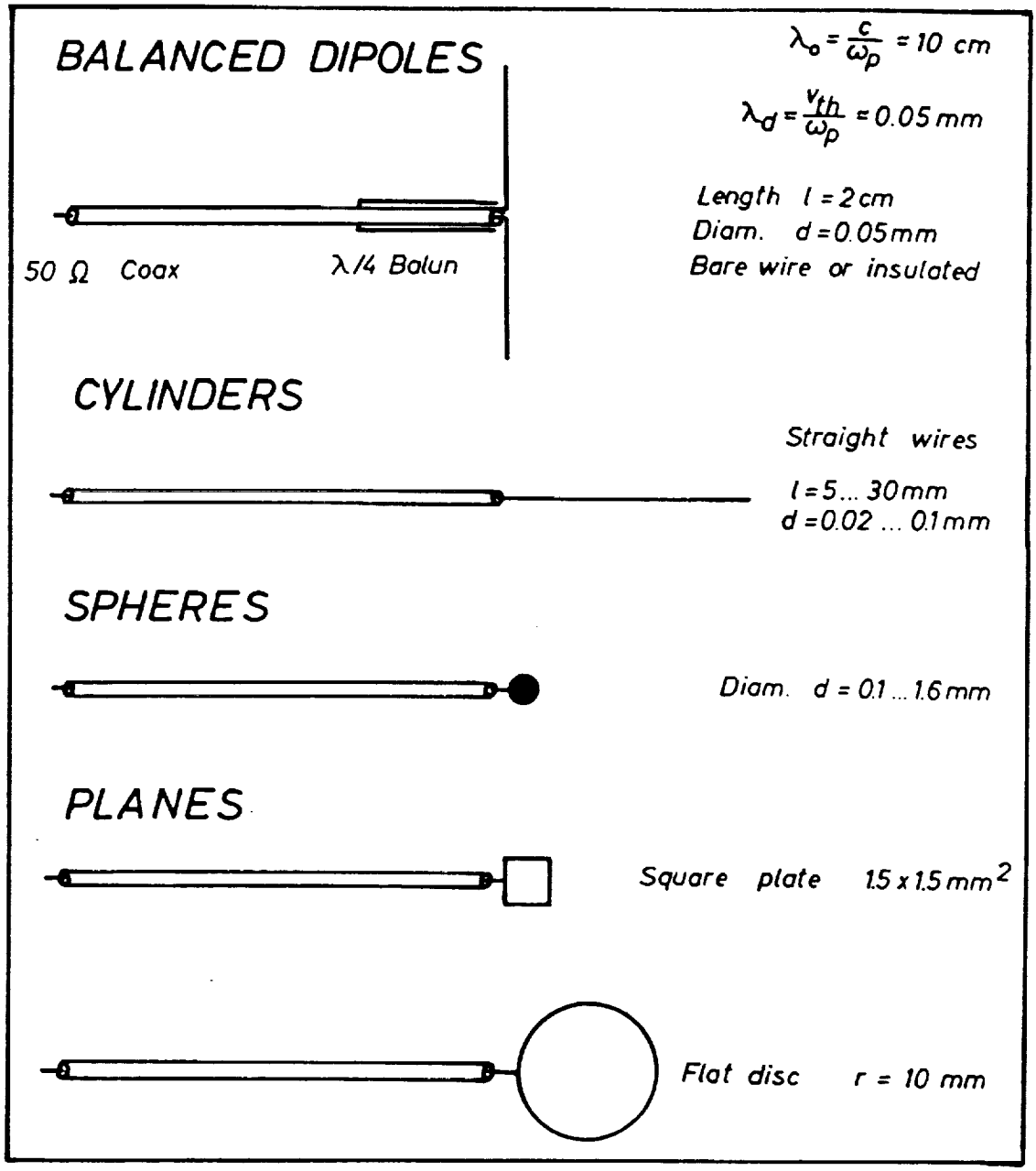
BALANCED DIPOLES
$\lambda_o = \frac{c}{\omega_p} = 10$ cm
$\lambda_d = \frac{v_{th}}{\omega_p} = 0.05$ mm
Length $l = 2$ cm
Diam. $d = 0.05$ mm
Bare wire or insulated
50 Ω Coax
λ/4 Balun
CYLINDERS
Straight wires
$l = 5 \ldots 30$ mm
$d = 0.02 \ldots 0.1$ mm
SPHERES
Diam. $d = 0.1 \ldots 1.6$ mm
PLANES
Square plate 1.5×1.5 mm^2
Flat disc $r = 10$ mm

Fig. 4

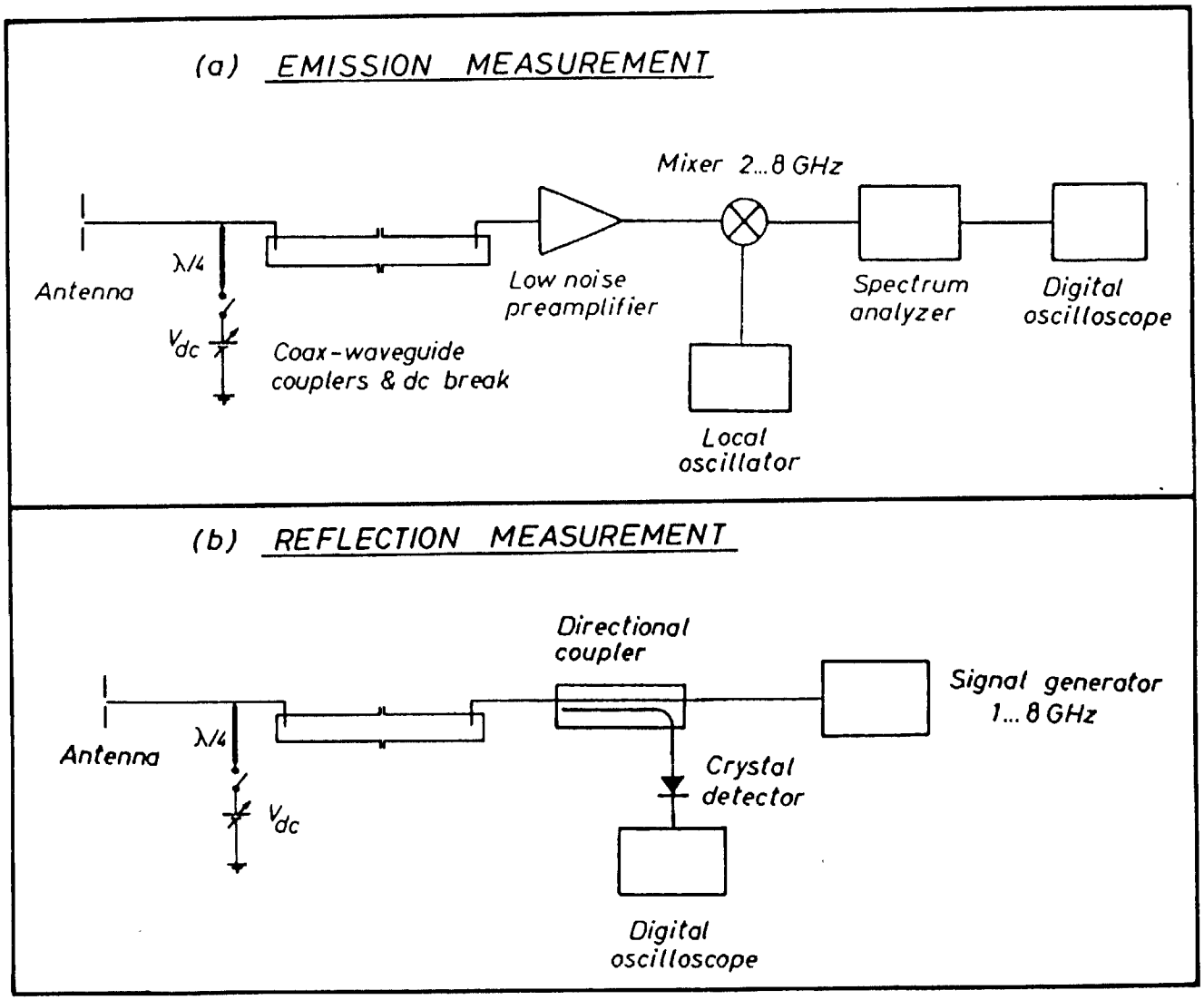
(a) EMISSION MEASUREMENT
Mixer 2...8 GHz
λ/4
Antenna
Low noise preamplifier
Spectrum analyzer
Digital oscilloscope
V_{dc}
Coax-waveguide couplers & dc break
Local oscillator
(b) REFLECTION MEASUREMENT
Directional coupler
Signal generator 1...8 GHz
λ/4
Antenna
Crystal detector
V_{dc}
Digital oscilloscope

Fig. 5

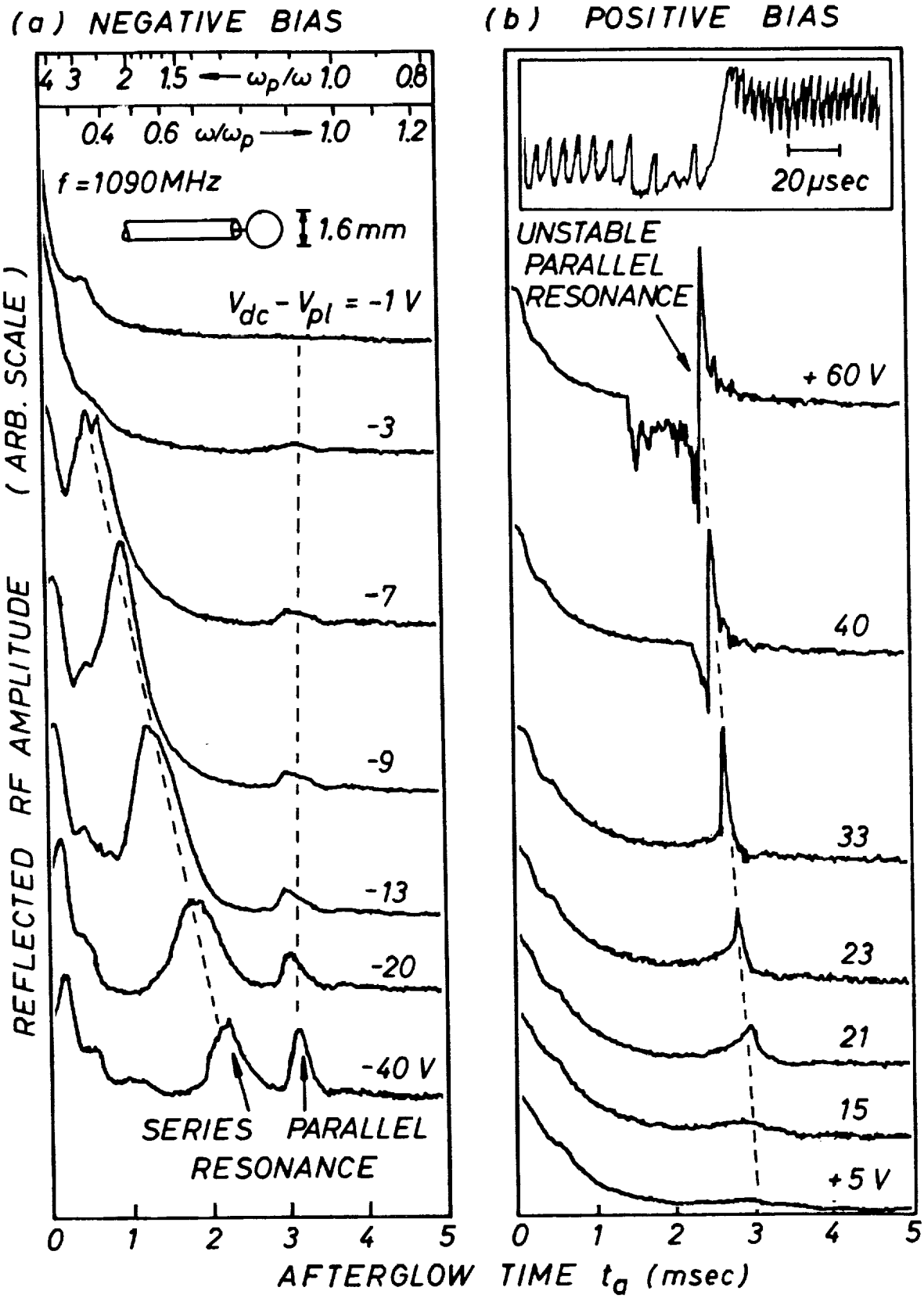
(a) NEGATIVE BIAS
(b) POSITIVE BIAS
4 3 2 1.5 ω_p/ω 1.0 0.8
0.4 0.6 ω/ω_p 1.0 1.2
f = 1090 MHz
1.6 mm
V_dc - V_pl = -1 V
-3
-7
-9
-13
-20
-40 V
SERIES RESONANCE
PARALLEL RESONANCE
20 μsec
UNSTABLE PARALLEL RESONANCE
+60 V
40
33
23
21
15
+5 V
REFLECTED RF AMPLITUDE (ARB. SCALE)
0 1 2 3 4 5
AFTERGLOW TIME t_a (msec)

Fig. 6

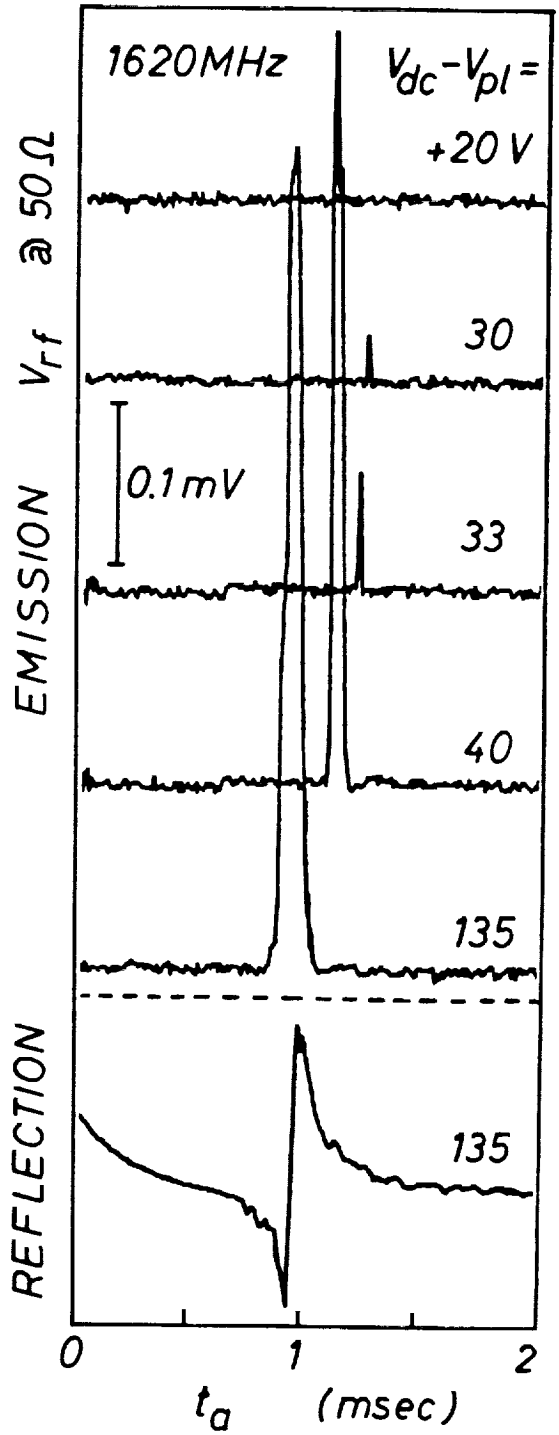
1620MHz
$V_{dc}-V_{pl}$ =
+20 V
30
33
40
135
135
0.1mV
EMISSION V_{rf} @ 50 Ω
REFLECTION
0
1
2
t_a (msec)

Fig. 7

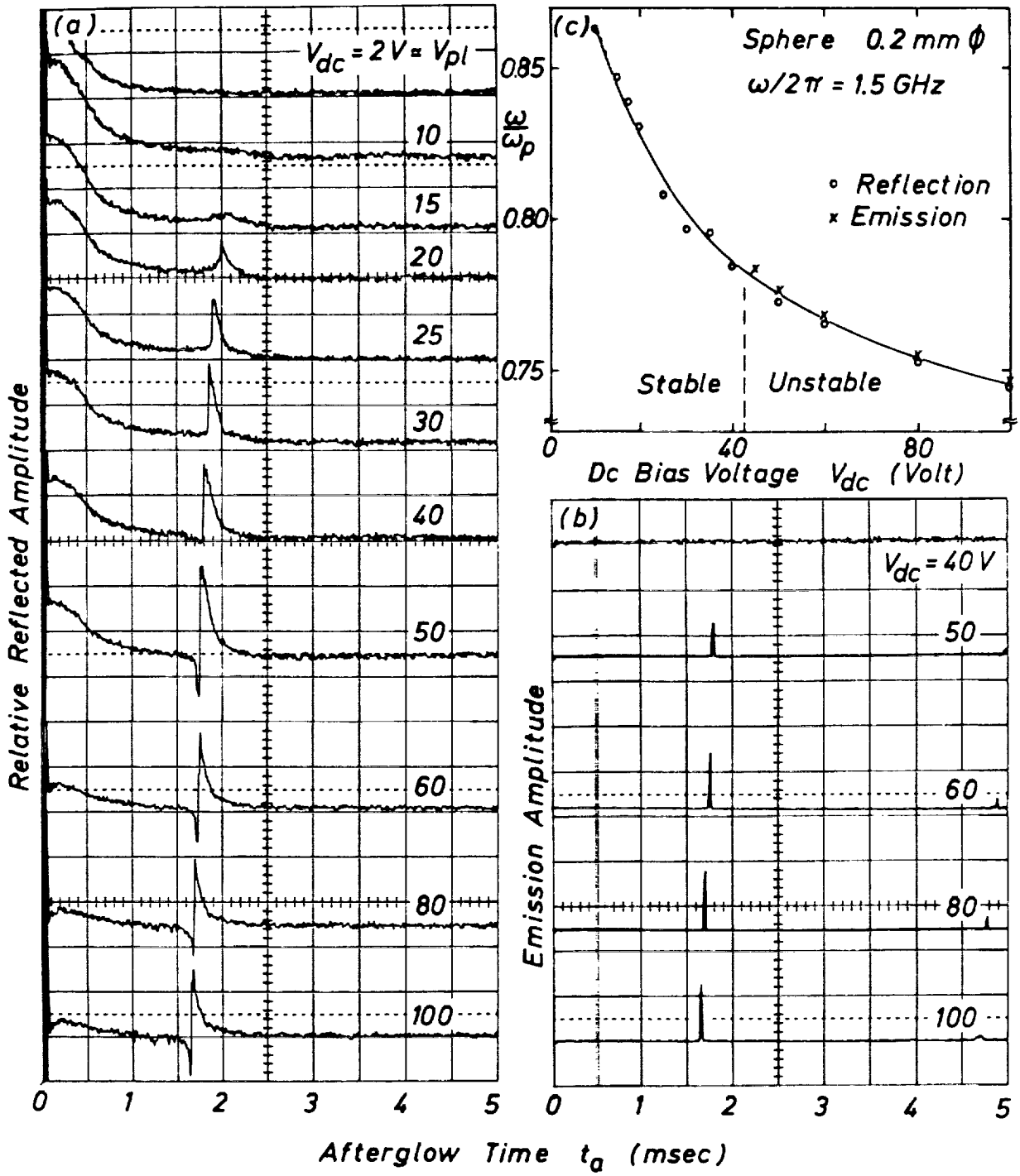
(a)
V_{dc} = 2V ≈ V_{pl}
10
15
20
25
30
40
50
60
80
100
0.85
0.80
0.75
ω/ω_p
Relative Reflected Amplitude
0
1
2
3
4
5
Afterglow Time t_a (msec)
(c)
Sphere 0.2 mm ϕ
ω/2π = 1.5 GHz
○ Reflection
× Emission
Stable
Unstable
0
40
80
Dc Bias Voltage V_{dc} (Volt)
(b)
V_{dc} = 40 V
50
60
80
100
Emission Amplitude

Fig. 8

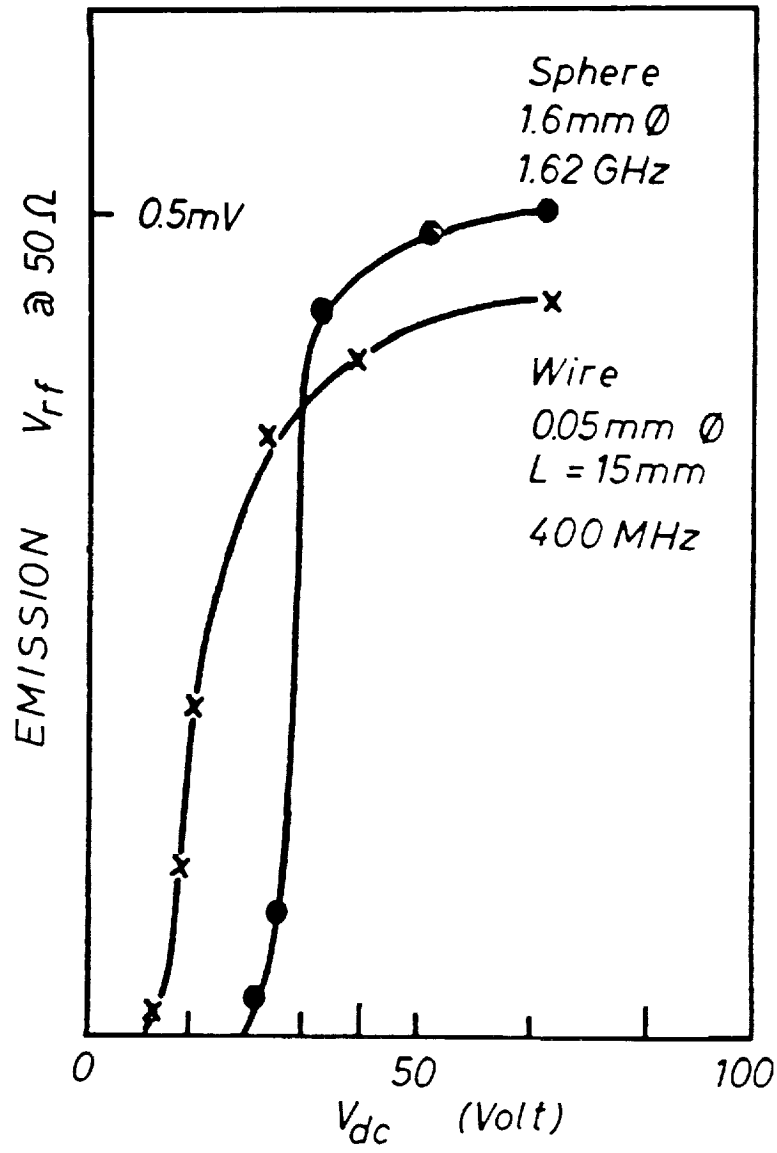
Sphere
1.6mm Ø
1.62 GHz
0.5mV
Wire
0.05mm Ø
L = 15mm
400 MHz
EMISSION V_{rf} @ 50Ω
0
50
100
V_{dc} (Volt)

Fig. 9

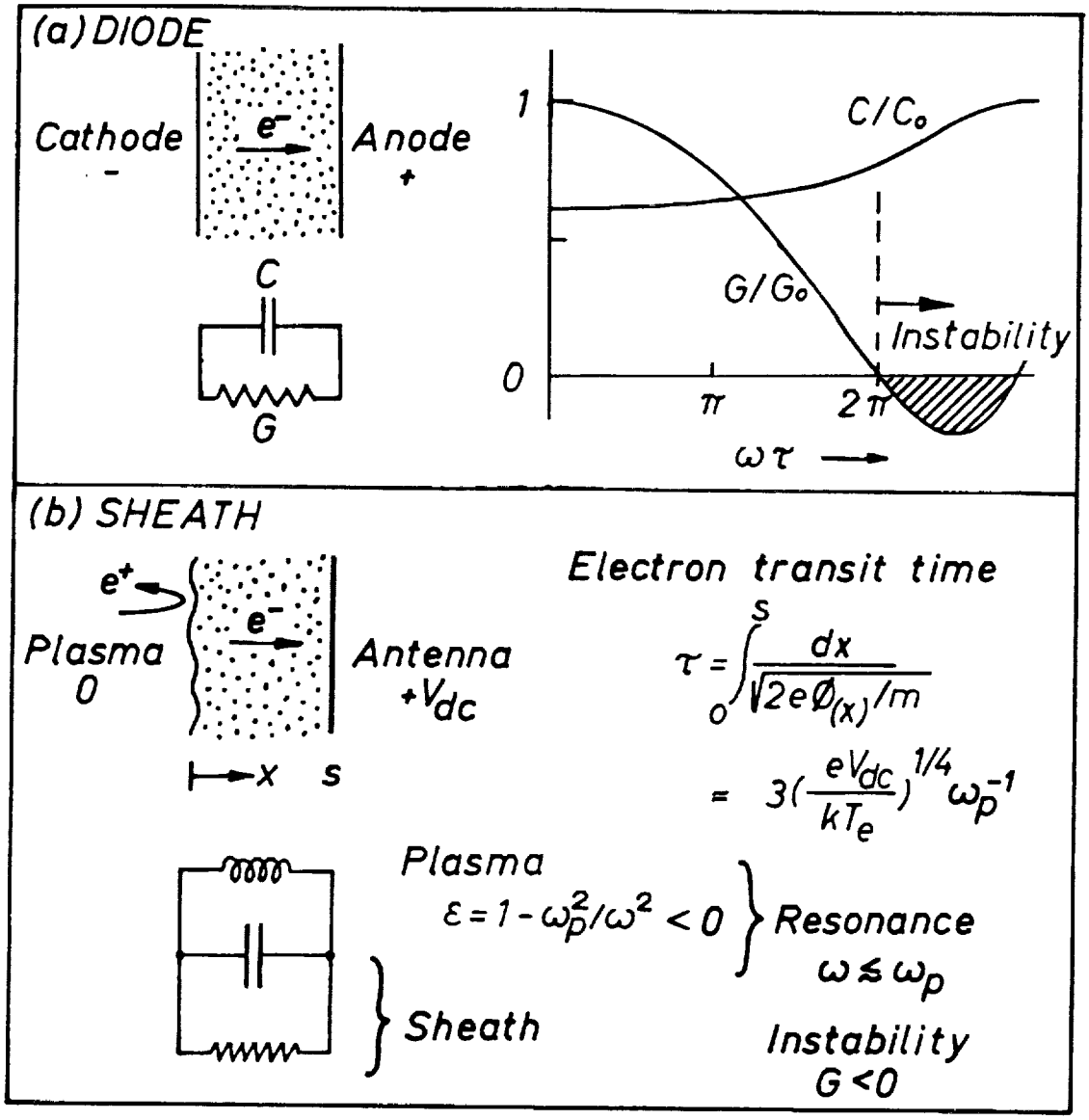
(a) DIODE
Cathode
-
e⁻
Anode
+
C
G
1
0
C/C₀
G/G₀
Instability
π
2π
ωτ
(b) SHEATH
e⁺
e⁻
Plasma
0
Antenna
+V_dc
x
s
Electron transit time
τ = ∫₀ˢ dx / √(2eØ(x)/m)
= 3(eV_dc/kT_e)^1/4 ω_p^-1
Plasma
ε = 1 - ω_p²/ω² < 0
Resonance
ω ≲ ω_p
Sheath
Instability
G < 0

Fig. 10

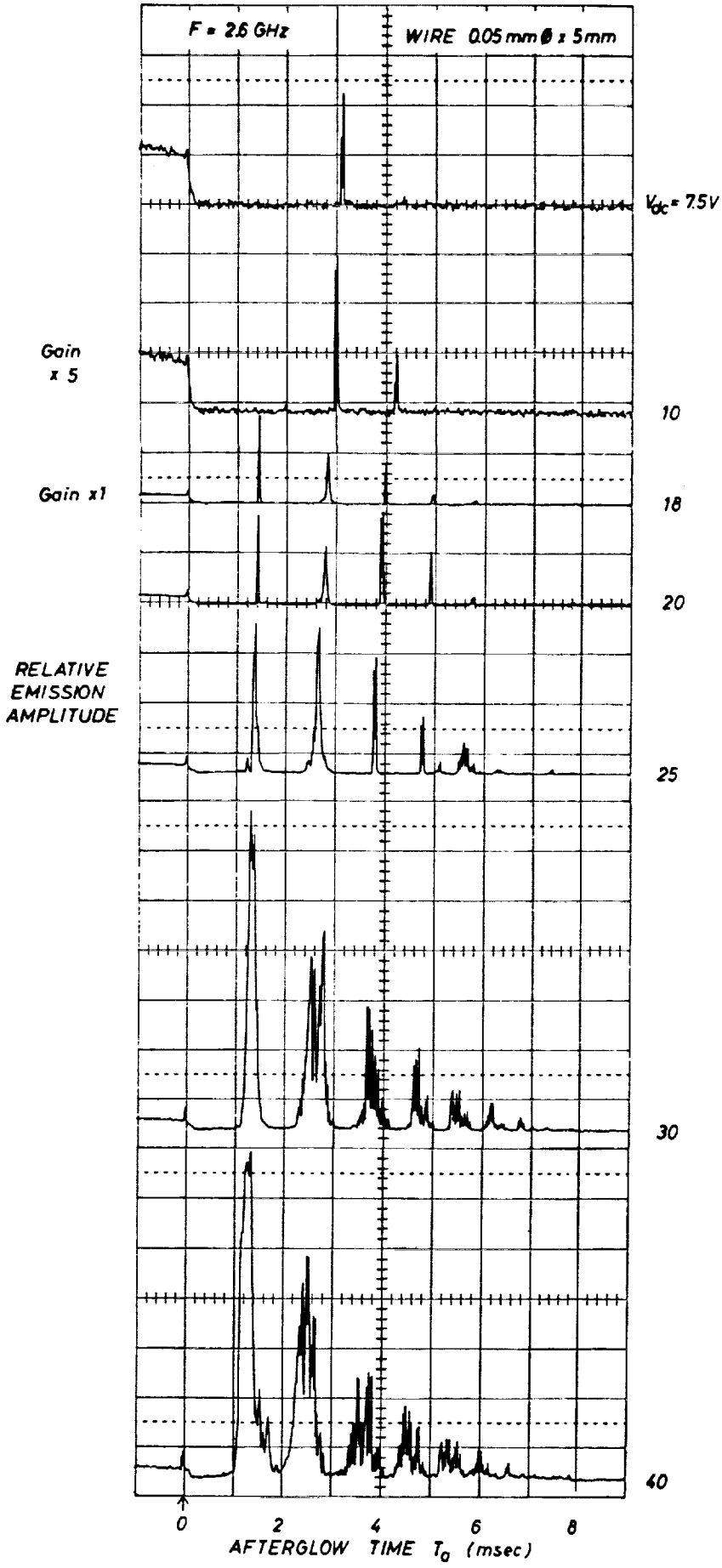
F = 2.6 GHz
WIRE 0.05 mm Ø x 5mm
V_{dc} = 7.5V
Gain x 5
Gain x1
10
18
20
RELATIVE EMISSION AMPLITUDE
25
30
40
0
2
4
6
8
AFTERGLOW TIME T_a (msec)

Fig. 11

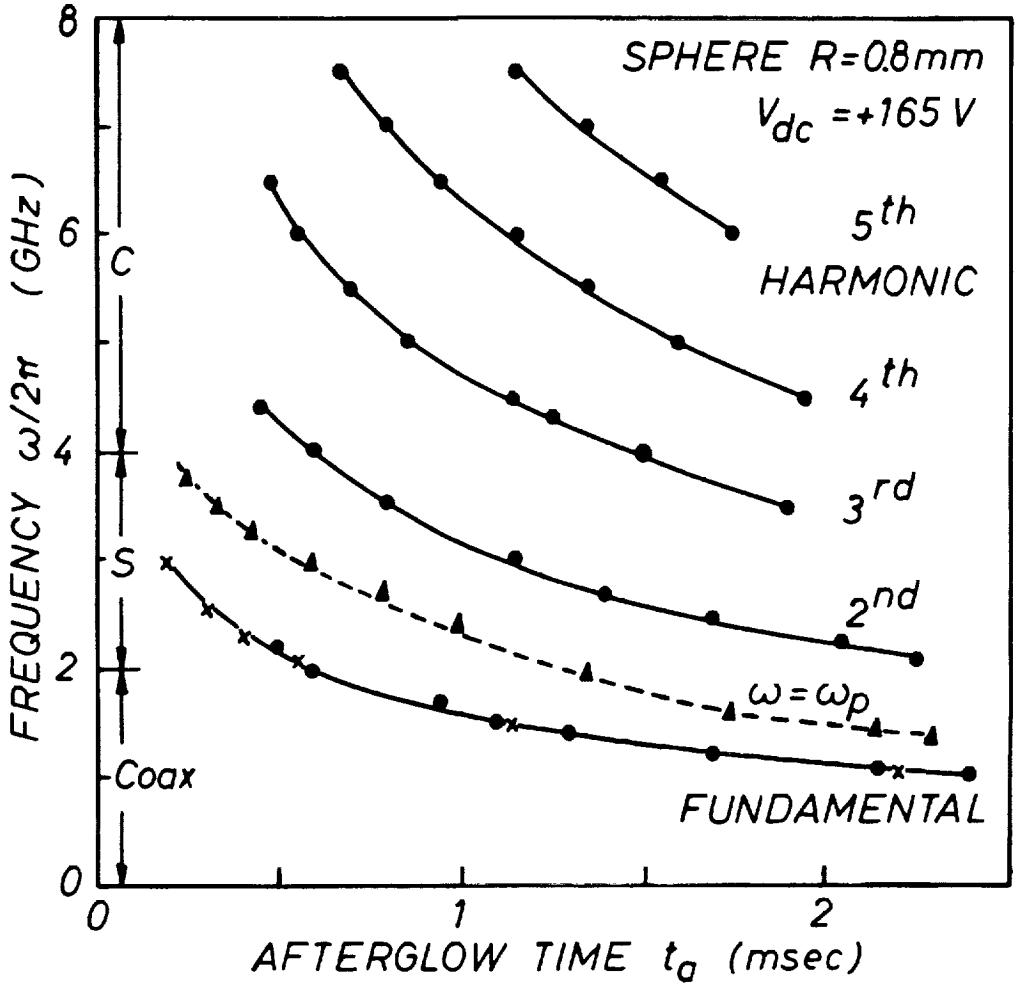
SPHERE R=0.8mm
V_{dc} =+165 V
5th HARMONIC
4th
3rd
2nd
ω=ωp
FUNDAMENTAL
C
S
Coax
FREQUENCY ω/2π (GHz)
AFTERGLOW TIME t_a (msec)
0
2
4
6
8
0
1
2

Fig. 12

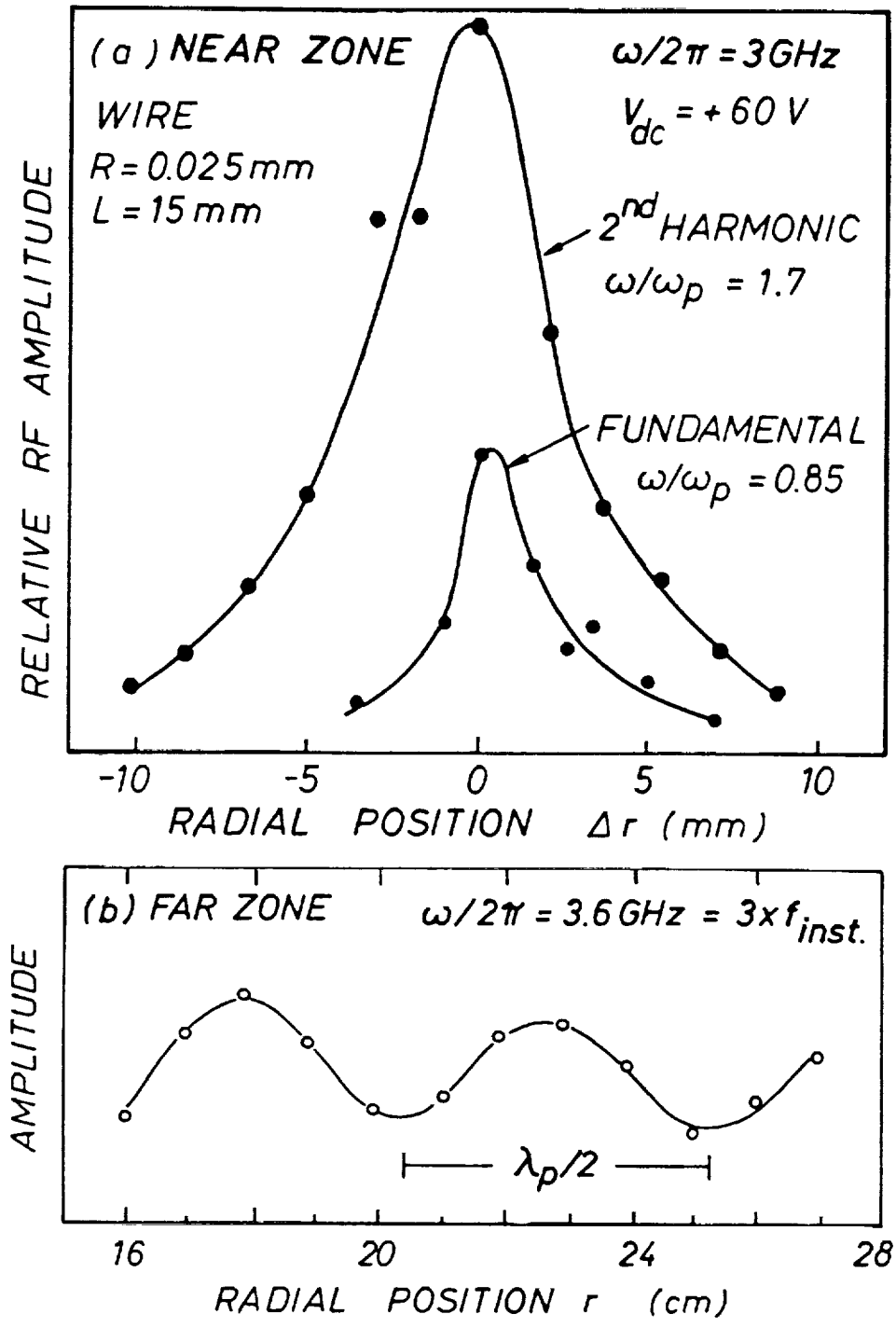
(a) NEAR ZONE
ω/2π = 3GHz
WIRE
R = 0.025mm
L = 15mm
V_dc = + 60 V
2nd HARMONIC
ω/ω_p = 1.7
FUNDAMENTAL
ω/ω_p = 0.85
RELATIVE RF AMPLITUDE
-10
-5
0
5
10
RADIAL POSITION Δr (mm)
(b) FAR ZONE
ω/2π = 3.6 GHz = 3x f_inst.
AMPLITUDE
λ_p/2
16
20
24
28
RADIAL POSITION r (cm)

Fig. 13

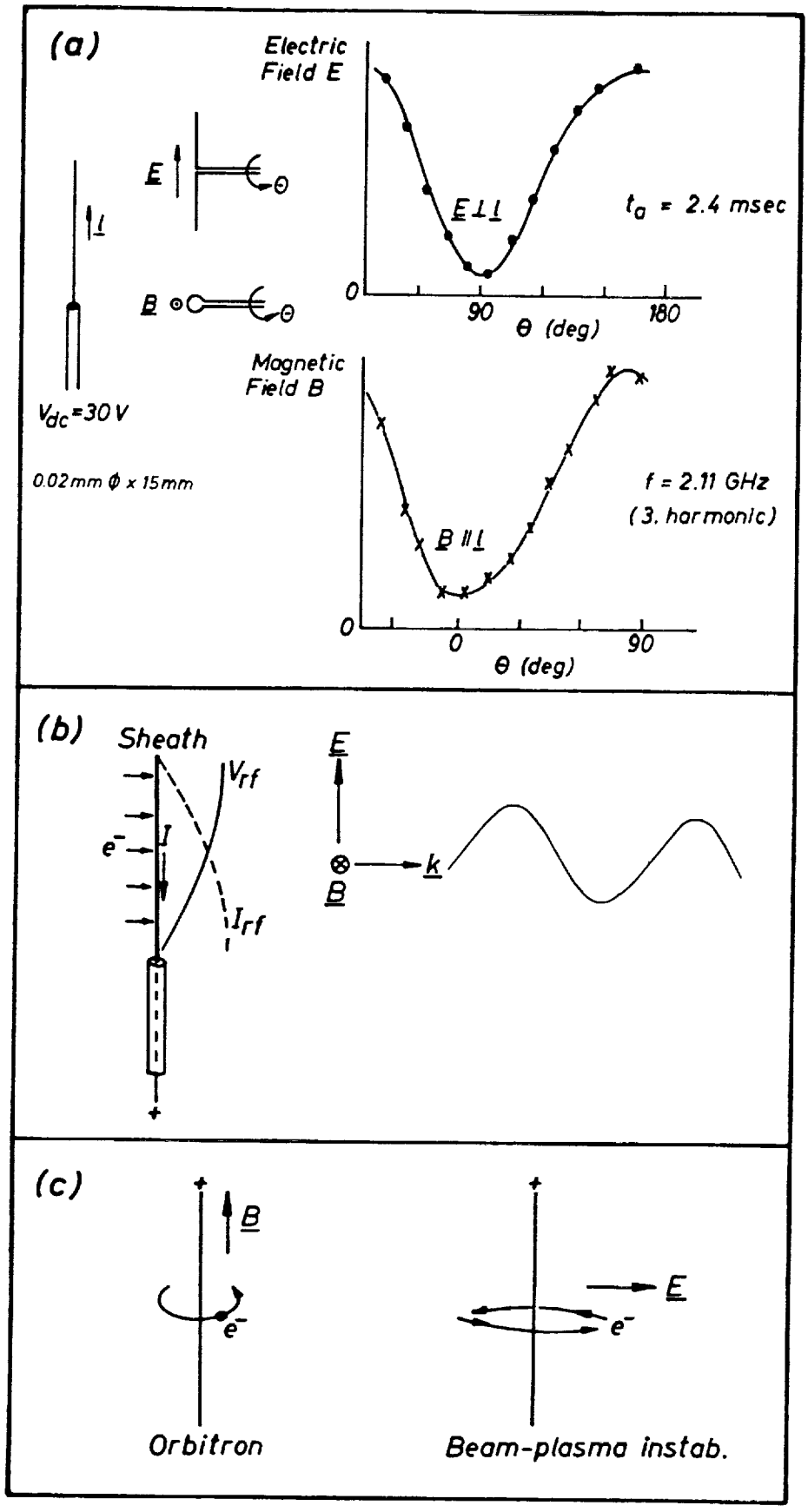
(a)
Electric
Field E
E
Θ
I
B
Θ
E ⊥ I
t_a = 2.4 msec
0
90
180
Θ (deg)
V_{dc}=30 V
0.02mm ϕ x 15mm
Magnetic
Field B
B ∥ I
f = 2.11 GHz
(3. harmonic)
0
0
90
Θ (deg)
(b)
Sheath
V_{rf}
e^-
I
I_{rf}
E
k
B
(c)
B
e^-
Orbitron
E
e^-
Beam-plasma instab.

Fig. 14

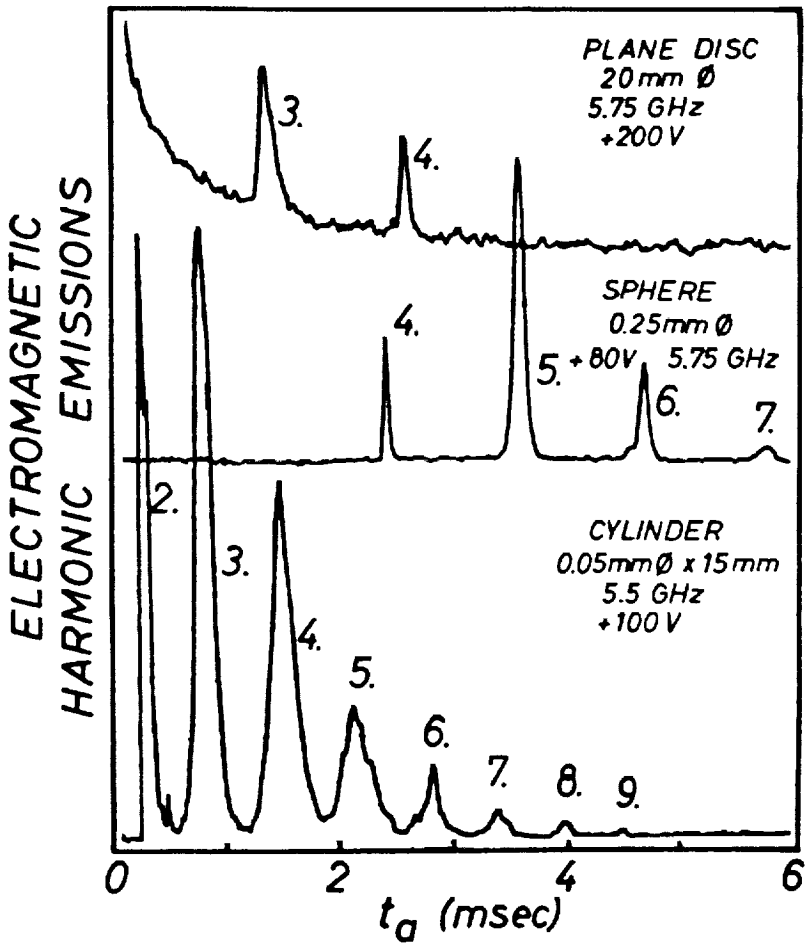
ELECTROMAGNETIC HARMONIC EMISSIONS
PLANE DISC
20 mm Ø
5.75 GHz
+200 V
3.
4.
SPHERE
0.25mm Ø
4.
5. +80V
5.75 GHz
6.
7.
2.
3.
CYLINDER
0.05mm Ø x 15mm
5.5 GHz
+100 V
4.
5.
6.
7.
8.
9.
0
2
4
6
t_a (msec)

Fig. 15

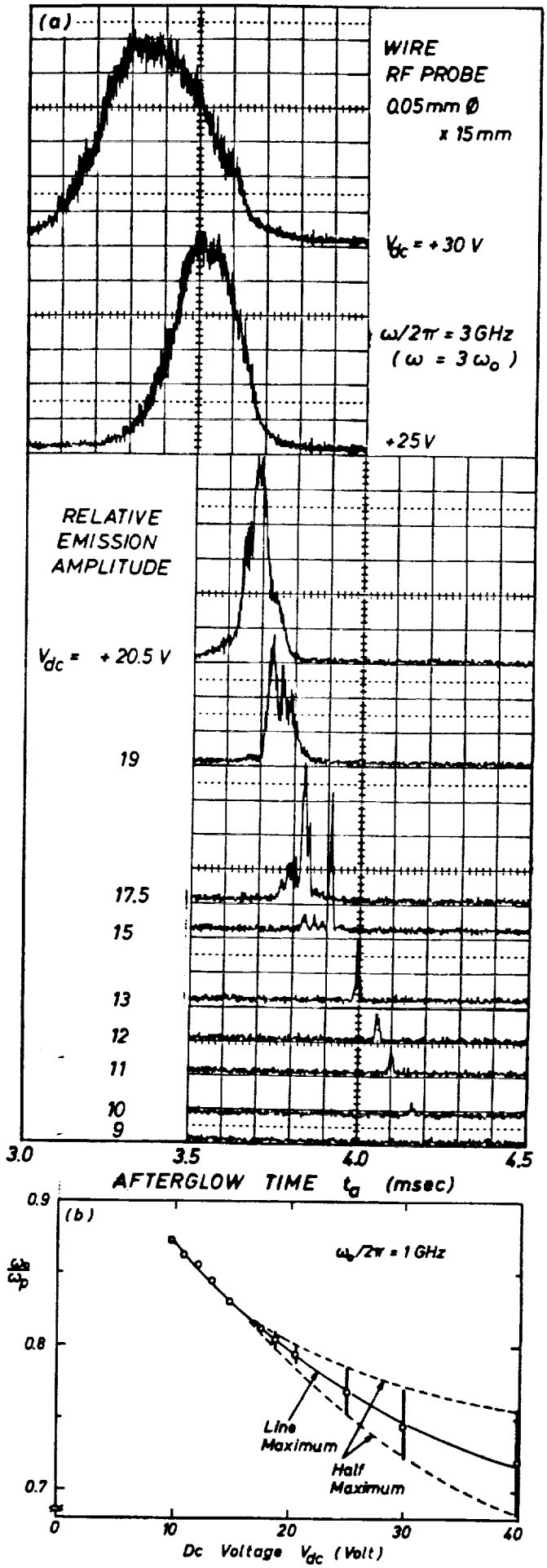
(a)
WIRE
RF PROBE
0.05mm Ø
x 15mm
V_{dc} = +30 V
ω/2π = 3GHz
(ω = 3ω₀)
+25V
RELATIVE
EMISSION
AMPLITUDE
V_{dc} = +20.5 V
19
17.5
15
13
12
11
10
9
3.0
3.5
4.0
4.5
AFTERGLOW TIME t_a (msec)
(b)
$\omega_b/2\pi$ = 1 GHz
$\frac{\omega_b}{\omega_p}$
0.9
0.8
0.7
Line
Maximum
Half
Maximum
0
10
20
30
40
Dc Voltage V_{dc} (Volt)

Fig. 16

HIGH TIME RESOLUTION MEASUREMENTS OF EMISSIONS

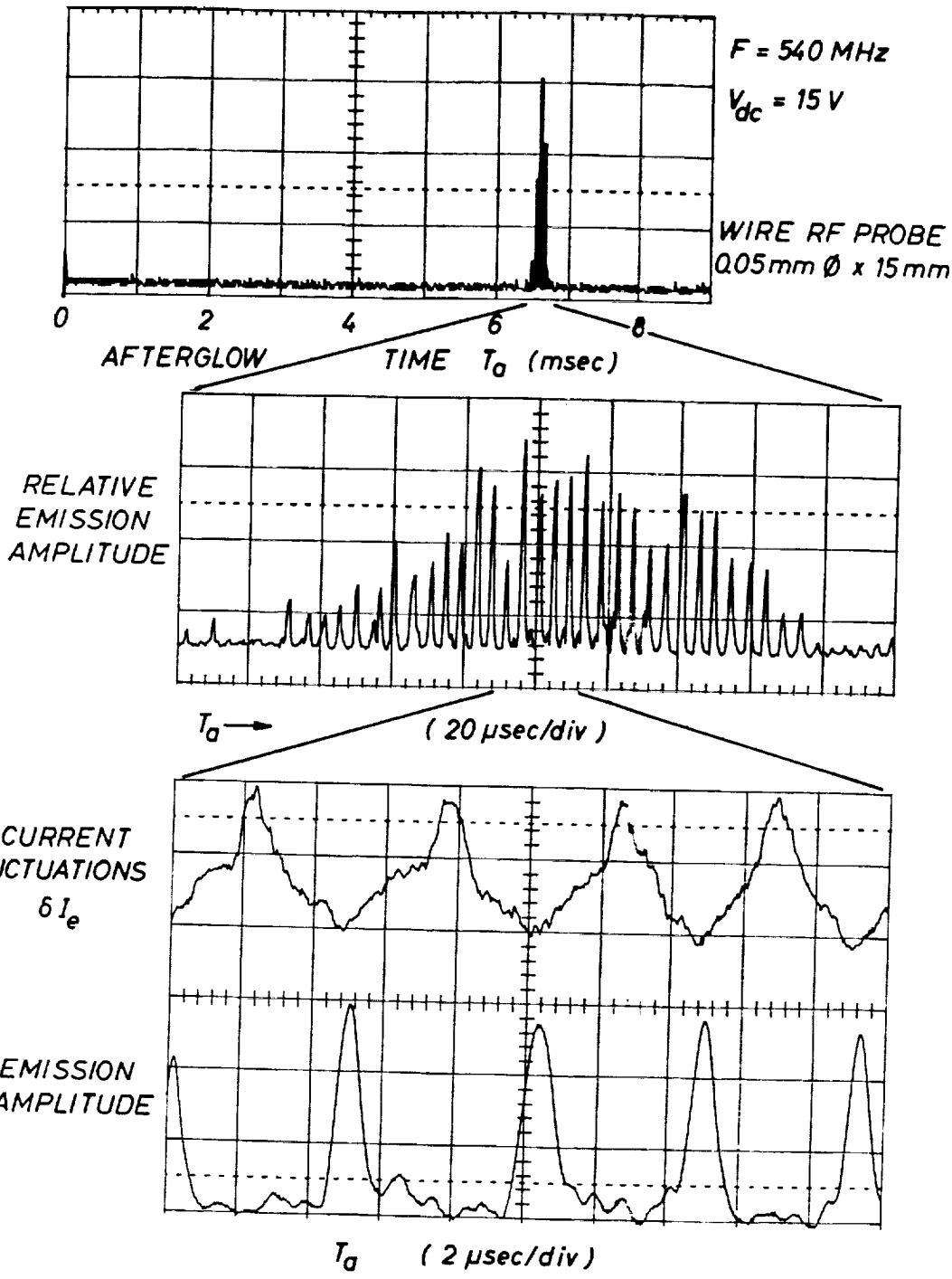

Fig. 17

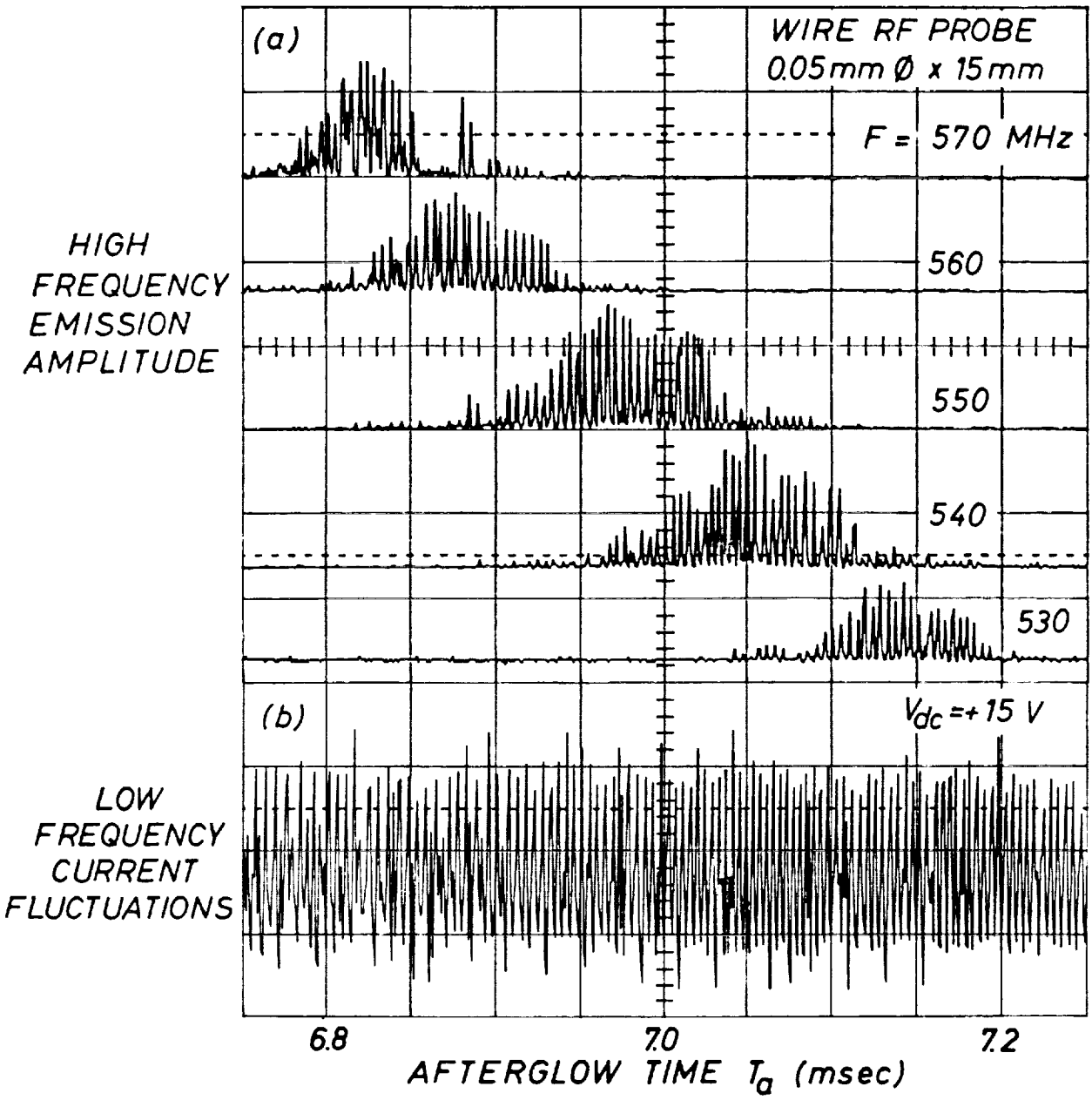
(a)
WIRE RF PROBE
0.05mm Ø x 15mm
F = 570 MHz
560
550
540
530
HIGH
FREQUENCY
EMISSION
AMPLITUDE
(b)
V_{dc} =+15 V
LOW
FREQUENCY
CURRENT
FLUCTUATIONS
6.8
7.0
7.2
AFTERGLOW TIME T_a (msec)

Fig. 18

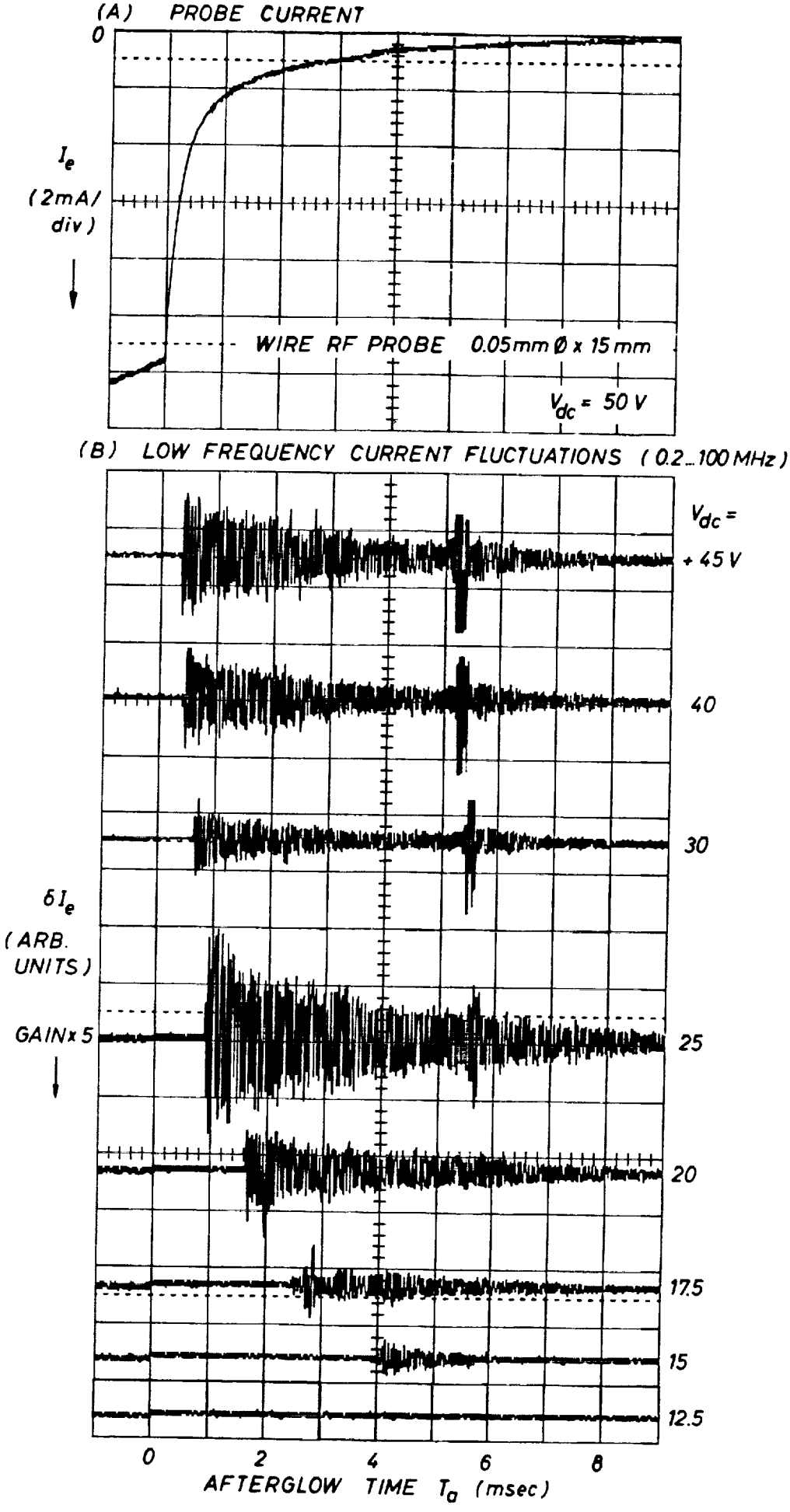
(A) PROBE CURRENT
0
I_e
(2mA/
div)
WIRE RF PROBE 0.05mm Ø x 15mm
V_{dc} = 50 V
(B) LOW FREQUENCY CURRENT FLUCTUATIONS (0.2–100 MHz)
V_{dc} =
+45 V
40
30
δI_e
(ARB.
UNITS)
GAIN x 5
25
20
17.5
15
12.5
0
2
4
6
8
AFTERGLOW TIME T_a (msec)

Fig. 19

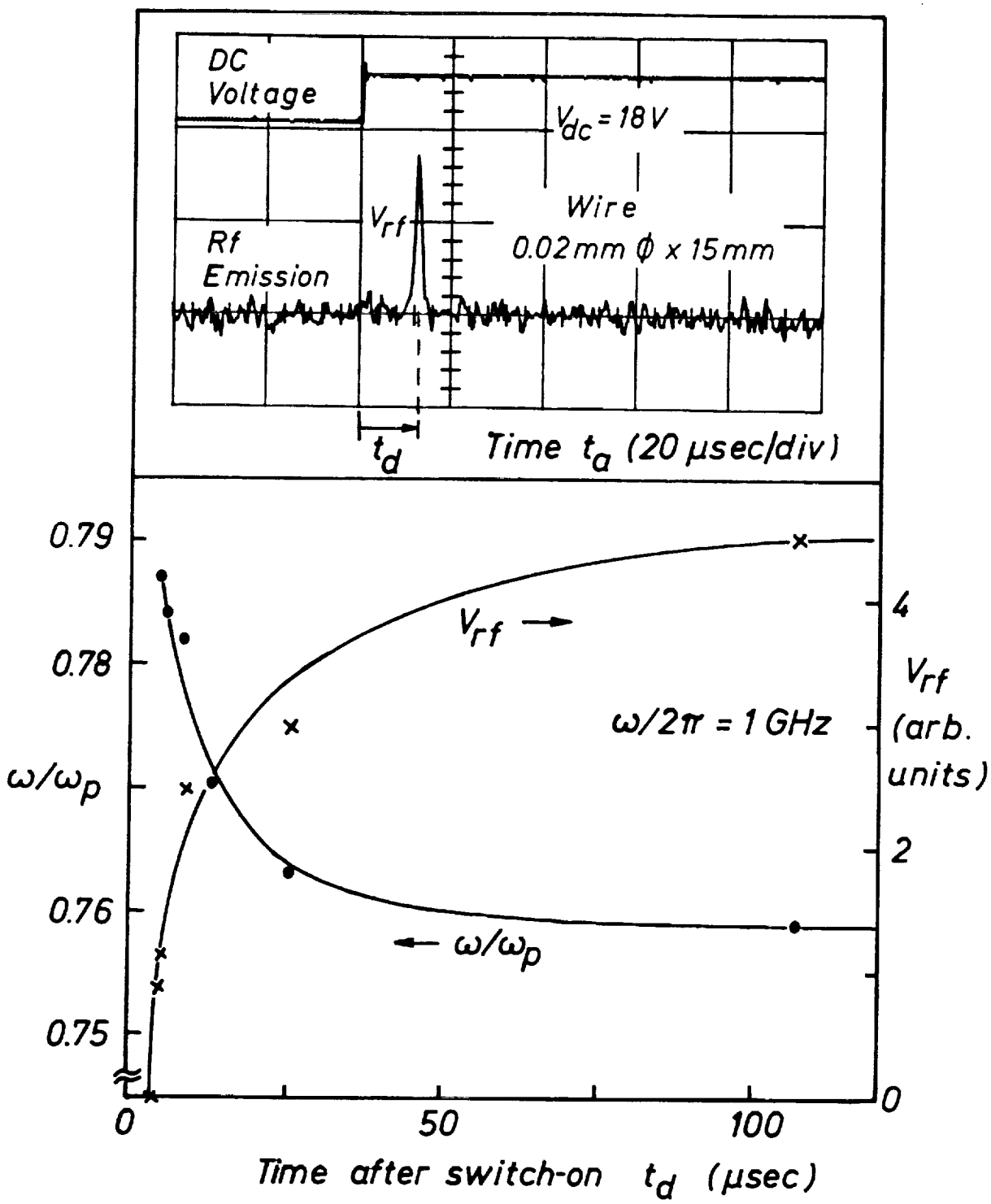
DC
Voltage
V_{dc} = 18 V
V_{rf}
Wire
0.02mm ϕ x 15mm
Rf
Emission
t_d
Time t_a (20 μsec/div)
0.79
0.78
0.76
0.75
ω/ω_p
V_{rf} →
$\omega/2\pi$ = 1 GHz
← ω/ω_p
4
2
0
V_{rf} (arb. units)
0
50
100
Time after switch-on t_d (μsec)

Fig. 20